博　士　論　文

Study on Regulatory Mechanisms of Osteoclasts Using the Zebrafish Fractured Scale

ゼブラフィッシュ骨折鱗を用いた破骨細胞の制御機構に関する研究

金沢大学大学院自然科学研究科

自然システム学専攻

学籍番号　　　　1724062004
氏　　名　　　　小林　静静
主任指導教員名　小林　　功
提出年月　　　　2021- 06- 25

The present thesis is based on the following original articles.

1. **Kobayashi-Sun J**, Suzuki N, Hattori A, Yamaguchi M, Kobayashi I*. Melatonin suppresses both osteoblast and osteoclast differentiation through repression of epidermal Erk signaling in the zebrafish scale. *Biochem Biophys Res Commun*. 530(4):644-650, 2020

2. **Kobayashi-Sun J**, Yamamori S, Kondo M, Kuroda J, Ikegame M, Suzuki N, Kitamura K, Hattori A, Yamaguchi M, Kobayashi I*. Uptake of osteoblast-derived extracellular vesicles promotes the differentiation of osteoclasts in the zebrafish scale. *Commun Biol*. 3(1):190, 2020

Abbreviations

OC	Osteoclast
OB	Osteoblast
EV	Extracellular vesicle
Trap	Tartrate-resistant acid phosphatase
TNFα	Tumor necrosis factor α
IL6	Interleukin 6
ALP	Alkaline phosphatase
VEGF	Vascular endothelial growth factor
RANK	Receptor activator of nuclear factor-κB
RANKL	Receptor activator of nuclear factor kappa-B ligand
OPG	Osteoprotegerin
M-CSF	Macrophage-colony stimulating factor
DC-STAMP	Dendritic cell-specific transmembrane protein
PTH	Parathyroid hormone
M-CSF	Macrophage colony stimulating factor
OVX	Ovariectomy
FCM	Flow cytometry

Table of Contents

Chapter 1

General Introduction

Bone is a connective tissue that generates a rigid framework to protect vital organs. In addition, it also functions as a reservoir for calcium, phosphorus, and magnesium and a niche for hematopoietic cells in the bone marrow (Morgan et al. 2008). Turnover of bone tissue is regulated by a fine balance between bone resorption and bone formation, and two types of cells are involved in these complementary processes in vertebrates, osteoclasts (OCs) and osteoblasts (OBs). Although the balance between these two types of cells is important for maintenance of bone tissues, bone resorption by OCs proceeds more rapidly compared with bone formation by OBs (Arnett and Orriss, 2018). Various bone disorders and diseases are caused by unbalanced bone resorption and formation, including substantial bone degradation by OCs and impaired bone formation by OBs. Defective OC activity leads to osteopetrosis, a bone disease that causes excessive bone density, while excess activation of OCs results in osteoporosis, a bone disease that causes a loss of bone density. Because OCs are derived from hematopoietic stem cells present in the bone marrow, bone marrow transplantation is partially effective to treat osteopetrosis (Stepensky et al., 2019). Due to an aging population and longer lifespan, osteoporosis has recently become a global epidemic disease. It has been estimated that more that 200 million patients are suffering from osteoporosis in the world (Tümay Sözen et al., 2017). Although patients with osteoporosis are generally treated with inhibitors for osteoclasts (e.g. bisphosphonates) as preventative treatment, it cannot be expected to completely care osteoporosis by these drugs. Furthermore, these drugs have been shown to have long-term side effects (Miyazawa et al., 2020). A better understanding of OC formation in vivo is therefore required for clinical therapies of osteoporosis.

In the clinical setting, the most common form of bone regeneration is fracture healing, which includes the formation and activation of OCs and OBs in a spatial and temporal

manner (Dimitriou et al. 2011). The following literature review consists of the overview of formation and roles of OCs in bone fracture healing, focusing on the advanced knowledge of regulatory pathways in either cell lines or model animals, followed by discussion on the research models involved in studies of OCs.

1. OC formation

1.1 Features of OCs

OCs are essential for bone resorption during the process of bone remodeling. Besides, OCs also play important roles in regulation of bone formation, intraosseous angiogenesis, and hematopoiesis (Cappariello et al., 2014).

Unlike OBs, which are mesenchymal origin and essentially reside in the bone tissue, the place and process of OC differentiation is still not fully understood (Drissi and Sanjay, 2016). Although it is widely recognized that OCs are differentiated from hematopoietic stem cells, recent studies have shown that OCs that colonize in fetal ossification centers originate from embryonic erythro-myeloid progenitors (Gomez Perdiguero et al., 2015; Jacome-Galarza et al., 2019). It is also known that OCs are differentiated not only from immature myeloid progenitors but also from mature monocytes and macrophages (Udagawa et al., 1990). OCs are terminally differentiated cells that are not capable of self-replication. Mononuclear OC precursors fuse to generate multinucleated mature OCs, get activated, and begin to bone resorption.

Activation of OCs includes cell polarization, including formation of a prominent ruffled border and clear zones at the site of attachment to the bone mineral. The expression of carbonic anhydrase 2 (CA2), vacuolar-type H+ ATPase (v-ATPase), cathepsin K (CTSK), and tartrate-resistant acid phosphatase (TRAP) markedly increases in clear

zones of mature OCs (Martin and Udagawa, 1998; Teitelbaum 2000). The average size of OCs is approximately 300 μm, containing eight nuclei on average, which is approximately 15 times larger than macrophages (Bar-Shavit, 2007). In some pathological conditions, OCs with more than 100 nuclei were reported (Tiedemann et al., 2017). Nuclei are generally localized in the vascular side of the cell, surrounded by endoplasmic reticula, in close of proximity of multiple Golgi apparatus and microtubule organization centers (Cappariello et al., 2014). Another typical feature of OCs is numerous mitochondria in their cell plasma, while the reason for the high number of mitochondria in OCs is unclear.

It is known that OCs have short lifespan (Arnett and Orriss, 2018; Soysa and Alles, 2019). Activated OCs in an adult human usually survive approximately 2~3 weeks and then undergo apoptosis, indicating that the number of OCs is controlled by the relative ratio of cell differentiation and cell death (Soysa and Alles, 2019).

1.2 Signal networks involved in osteoclastogenesis

Differentiation of myeloid progenitors into mature OCs are mainly regulated by Receptor activator of nuclear factor-κB ligand (RANKL, encoded by *TNFSF11*) and Macrophage colony-stimulating factor (M-CSF, encoded by *CSF1*), which are expressed by OBs, osteocytes and immune cells (Suda et al., 1999, Amarasekara et al., 2018) (Fig 1.1). During the early stage of OC differentiation, M-CSF induces proliferation and differentiation of OC precursors via Akt and ERK activation. Thereafter, RANKL induces differentiation of OC precursors into mature OCs through activation of the NF-κB, AP-1, CREB, MITF, and NFATc1 via TRAF6 recruitment and the MAPKs, Akt, Vav3 and c-Src signaling cascades. RANKL signaling is further strengthened by the TREM2- or OSCAR-

mediated signaling pathway through induction of a DAP12 / FcRγ / Syk / PLCγ signaling cascade that activates calcium signaling and NFATc1 induction (Amarasekara et al., 2018). In addition, proinflammatory cytokines (e.g. TNF-α, IL-1, and IL-6) induce OC differentiation, whereas anti-inflammatory cytokines (e.g. IL-4, IL-10, IFN-α, and IFN-β) inhibit osteoclastogenesis (Amarasekara et al., 2018).

Research on signaling pathways regulating OC differentiation is crucial for a comprehensive understanding of bone tissue under pathological conditions. Although some essential signaling pathways for OC differentiation have been identified, future studies of regulatory networks involved in bone resorption and formation are needed for developing therapeutic strategies, including the mechanisms underlying RANKL-mediated activation of OCs.

1.3 Hormones

Hormones indirectly control formation of OCs from myeloid precursors by acting upon OBs and, in some cases, also upon immune cells (Martin and Udagawa, 1998). Once OCs are formed in the presence of OBs, hormones, such as calcitonin and estrogen, do not regulate the activity of OCs, but they rather influence OC survival (Soysa and Alles, 2019).

The parathyroid hormone (PTH) family, including PTH and PTH-related peptide (PTHrP), regulate bone homeostasis through controlling the calcium level in blood via its receptors (PTHRs). It is widely known that PTH indirectly regulates osteoclastogenesis by activating PTH1R in OBs or osteocytes to increase the expression of RANKL (Romero et al., 2010). Recently, it has been shown that PTH1R is expressed by OCs and bovine PTH directly enhances bone resorption of OCs in vitro by modulating the expression and activity of v-ATPase subunits (Liu et al., 2016).

Melatonin is an avirulent indoleamine that controls circadian rhythms in vertebrates, but is also involved in osteoclastogenesis. Pharmacological dose of melatonin (1~100 μmol/L), but not physiological concentration (0.01~10nmol/L), significantly inhibits osteoclastogenesis by monocytes in the bone marrow via repression of the ROS-mediated pathway (Zhou et al., 2017; Kim et al, 2017). Since the melatonin level in blood is known to be reduced by aging, melatonin is a potential candidate to inhibit osteolysis in osteoporosis patients.

2. Research models for osteoclastogenesis

A number of cell culture assays for OBs and OCs can be used for a high throughput test on pharmaceuticals to treat bone diseases including osteoporosis. Primary murine or other mammalian bone marrow cells or peripheral blood precursors are often utilized to study the effect of a variety of factors/conditions on OC differentiation. OCs can easily be obtained in vitro from monocytic precursors in the presence of M-CSF and RANKL (Lacey et al., 1998; Shalhoub et al., 2000). However, such approaches have several limitations, including the difficulty to reflect the complex tissue interactions required for bone homeostasis and to predict the clinical output and performances. Thus, animal models, including rodent animals and fish are required to get a comprehensive understanding of osteoclastogenesis regarding physiological and pathological conditions to establish novel and effective clinical therapies (McKee et al., 1992; Erben, 1996; Zhou et al., 2010a; Martini et al., 2001; Ripamonti et al., 2001; Gunther and Schinke, 2000; Gomes and Fernandes, 2011; Caraguel et al., 2016; Lleras-Forero et al., 2020; Valenti eti al., 2020; Dietrich et al., 2021). Various models are summarized in Table 1.

2.1 Rodent models

During decades, bone researches have been mainly focused on mammalian animals (e.g. dogs, sheep, rabbits, rats, and mice) (O'Loughlin et al., 2008; Gomes and Fernandes, 2011). Compared to larger animals, mice own many advantages as a model organism for skeletal research, including relatively reasonable husbandry costs, short reproductive cycle, high conservation with human in genomic background, easiness in knock-in and knock-out genomic handling, and availability of antibodies against broad target molecules. The genetic background of mice influences the bone regeneration process and the phenotype; therefore, the age, gender, strain and genetic manipulation should be considered for bone research (Haffner-Luntzer et al., 2016).

The most popular model for studies of OC differentiation in rodents is the osteoporosis model, either by surgical manipulation, such as ovariectomy (OVX) in female mice, or by diet modification or drug administration, such as steroids (Egermann et al., 2005; Li et al., 2015). Ovariectomized mice are utilized as a model of osteoporosis, showing a rapid bone loss and delayed fracture healing due to the lack of ovary-derived estrogen (Beil et al., 2010), which is known to promote bone formation (Martin and Udagawa, 1998). The mouse is also a valuable model for age-related osteoporosis, because aging mice also show a progressive decrease in total bone mass like aging humans (Histing et al., 2013). Besides, some researchers intended to study osteoclastogenesis using fracture animals (Bahney et al., 2019; Zhang et al., 2019). The mouse calvarial defect model permits evaluation of drugs, growth factors, or cell transplantation efficacies, together with offering the benefit of utilizing genetic models to study intramembranous bone formation within defect sites (Samsonraj et al., 2017). Recently, the immune-deficient mice have been used for xenograftment of a human immune system by injection of human

hematopoietic stem cells. These chimeric mice are termed as 'humanized mice' in order to study the roles of specific cell types in vivo (Safinia et al., 2016). For example, it is possible to study the metastasis mechanisms of human cancer cells or some human virus-induced osteoclastogenesis using this xenograft model (Holzapfel et al., 2014; Nagasawa et al., 2021).

Based on the physical properties of the bone, many studies assess the effect in the bone via measurements of bone volume and density using techniques such as X-ray or computed tomography (CT) analysis (McGovern et al., 2018). Additionally, histological analysis and immunochemistry are also widely used to reveal the key molecules involved in OCs differentiation. Although it is extremely difficult to perform live imaging of OCs and OBs in vivo using mammalian models, a few studies successfully captured the dynamics of OCs and OBs using intravital two-photon microscopy. Nevius et al. reported that small mobile pre-osteoclasts migrated from the bone marrow towards the bone surface and then fused with already-existing OCs (Nevius et al., 2015). Furuya et al. demonstrated that direct cell-cell contact between mature OBs and OCs dynamically controls their function in vivo (Furuya et al., 2018).

Despite many advantages, attempts to minimize the utilization of rodents and other mammals are encouraged in accordance with 3R principles (replacement, reduction and refinement) in research (Morrison, 2002; Franco and Olsson, 2014). Therefore, non-mammalian animal models, in which disease parameters can be phenocopied or the effects of new medicines can be investigated, have gained high interests in the last decades.

2.2 Fish models

There are many similarities between mammalian and fish bone in terms of physiology and morphology (Fig 1.2). For instance, bone can be formed either via endochondral ossification or via intramembranous ossification (Hall 2005; Mackie et al., 2011). In mammals, the endoskeleton is typically formed via endochondral ossification and only a few bones, like the flat bones of the skull and the clavicle, formed by intramembranous ossification. In zebrafish, although endochondral ossification also occurs in a few bones (Weigele and Franz-Odendaal, 2016), intramembranous ossification plays important role for the endoskeleton system (Bird and Mabee, 2003). Especially, the dermal skeletal tissues, such as scales and fin rays, which have been reported to originate from mesodermal cells, rely only on intramembranous ossification (Ho Lee et al., 2013; Shimada et al, 2013).

Large clutches and the small body size in zebrafish and medaka enable high-throughput screens to identify therapeutic compounds (Mathias et al., 2012; Bergen et al., 2019; Fleras-Forero et al., 2020). In addition, fracture in skull, jaw, fin ray and scales of adult fish have demonstrated remarkable similarities and conservations in the major signaling pathways and key regulators of skeletal cells with mammals (Geurtzen et al., 2014; Takeyama et al., 2014; Stewart et al., 2014; Blum and Begemann, 2015; Park et al., 2016; Paul et al., 2016; Dietrich et al., 2021). Most importantly, the establishment of gene editing approaches via targeted endonuclease activity such as CRISPR/Cas9 or TALEN, further improves the applicability of organisms amenable to genetics (Witten et al., 2017). Teleost fish, particularly zebrafish and medaka, allow us to image skeletogenesis and the crosstalk between bone cells in vivo using a fluorescently labeled transgenic animals. Analysis of osteoclastogenesis and function in both zebrafish and medaka have shown

that OCs share common developmental specification and genetic controls with mammals (Witten et al., 2017). A type II diabetes model of zebrafish has been recently generated to analyze bone complications using scales. This model zebrafish showed an osteoporosis-like phenotype, suggesting that bone complications share the same mechanisms in humans and fish (Carnovali et al., 2016). A medaka osteoporosis model was recently generated based on inducible expression of Rankl (Phan et al., 2020). The data reveal that a chemokine Cxcl9l and its receptor Cxcr3.2 are essential to control the recruitment and differentiation of OC progenitors at bone resorption sites. Moreover, inhibition of Cxcr3.2 showed the protective effect of osteoporotic insult, indicating that targeting recruitment, rather than activation, of OC progenitors could be another choice for pharmacological treatment of osteoporosis.

3. Aim of the thesis

Compared with other models involved in bone research as mentioned above, zebrafish scales are available in large numbers and easily manipulated in vivo and in vitro. Scales can regenerate perfectly so that the animal can keep alive during the whole fracture healing process without suffering discomfort like rodent animals. Most importantly, scales provide OBs and OCs which attached to the matrix and can offer invaluable chances to directly monitor the interaction between OBs and OCs in vivo. The object of this thesis is to establish a zebrafish scale model that can be utilized for bone research and to elucidate novel regulatory mechanisms underlying osteoclastogenesis.
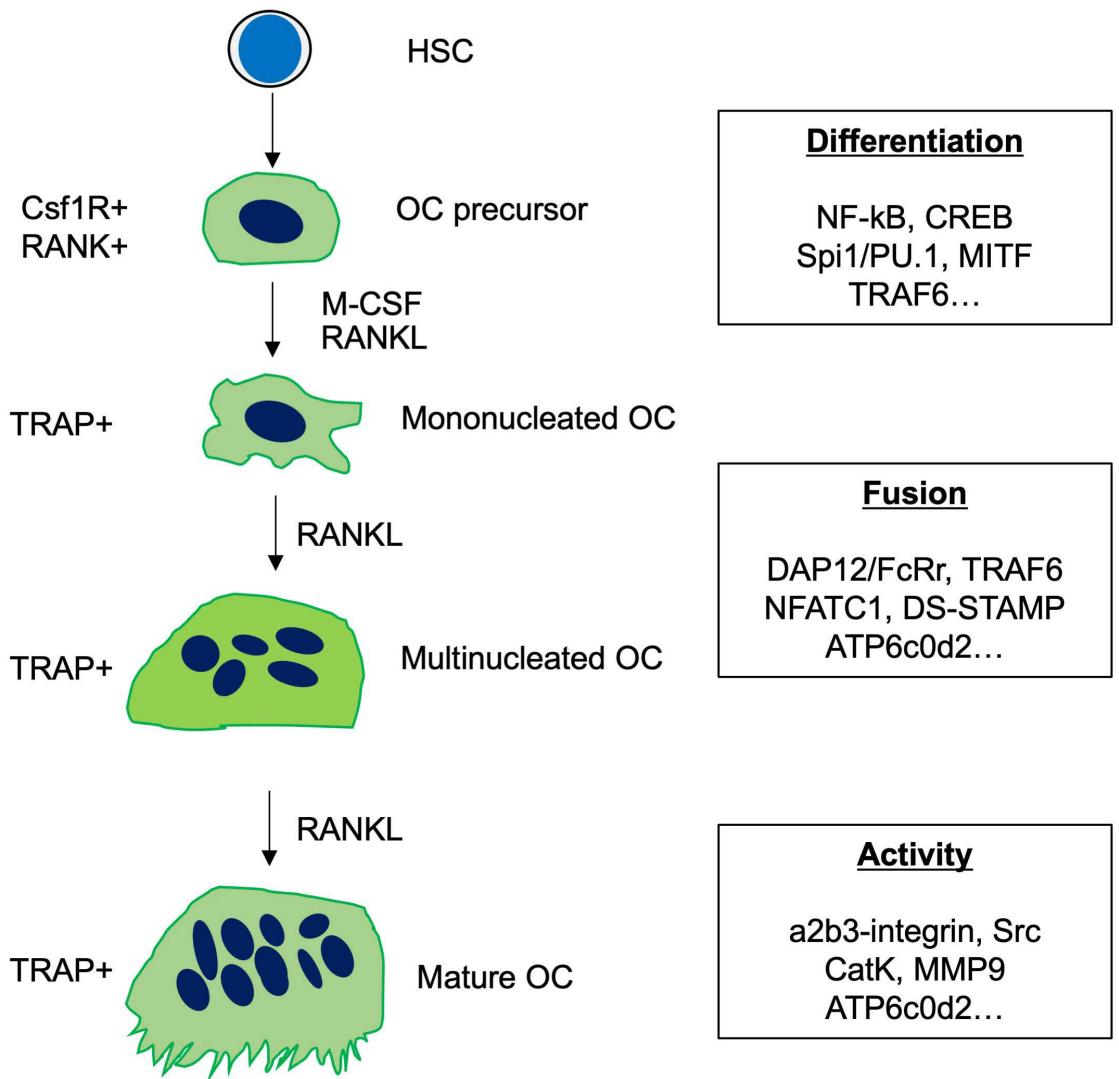
Figure 1.1 OC formation and differentiation.

Cartoon illustrating the process and signals of OC differentiation from the hematopoietic stem cells. HSC: hematopoietic stem cell; OC: osteoclast.
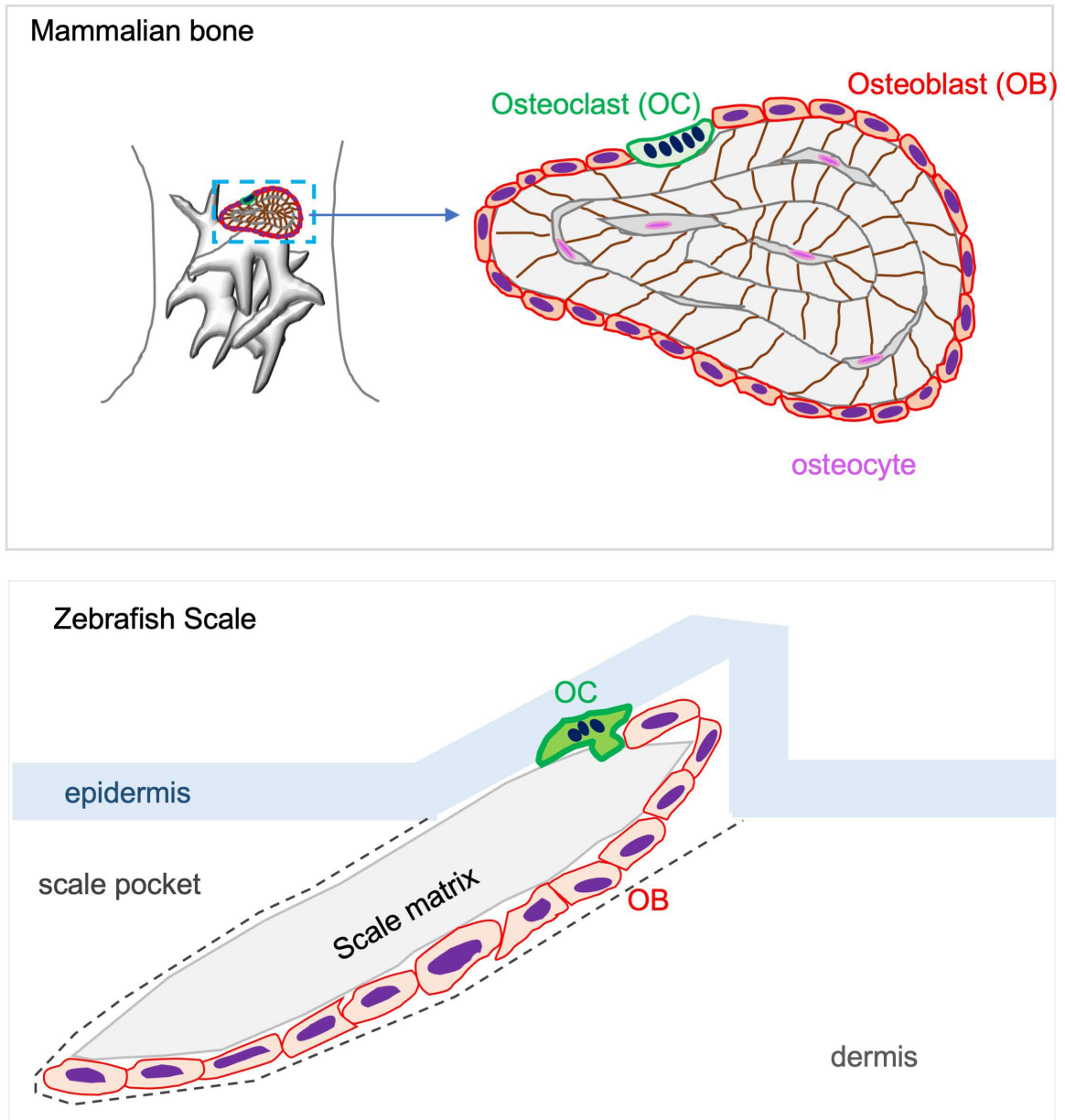
Figure 1.2 Schematic cross-section of a mammalian bone tissue and zebrafish scale.

OBs, osteocytes, and OCs locate in the bone surface. The scale is obliquely positioned in the scale pocket in the dermis and covered by the epidermis. OB, osteoblast. OC, osteoclast.

Table 1 Rodent and fish models in osteoclatogenesis

Type	Description	Ref
Transgenic lines	Tnfrsf11a:Cre (OC precursor)	Maeda et al., 2012
	Itgam:Cre (OC precursor)	Ferron and Vacher, 2005
	Lyz2:Cre(OC precursor)	Martin-Millan et al., 2010
	Acp5:Cre (preosteoclast)	Chiu et al., 2004
	Ctsk:Cre (OC)	Nakamura et al., 2007
Mutant	RANKL (knockout)	Kong et al., 1999; Lacey et al., 2000; Petti et al., 2001; etc.
	OPG (knockout)	Koide et al., 2013
	Rank (knockout)	Dougall et al., 1999; LI et al., 2000. etc.
	Atp6v0d2 (knockout)	Lee et al., 2006
	Ostm1 (Knockout)	Vacher et al., 2020
Osteoporosis	Ovarietomy (mouse, rat)	Jilka et al., 1992; Li et al., 1997; Smith et al., 2009 etc.
	Age-related	Farr et al., 2017; Lee et al., 2021; etc.
	glucocorticoid-induced (mouse, rat, rabbit)	Aerssen et al., 1994; Canalis et al., 2007; etc.
	Diabetes	Fajaro et al., 2017; etc.
	Rheumatoied arhritis	Engdahl et al., 2017; Hasegawa et al., 2019; etc.
	Cancer metastasis	Behzatoglu, 2021; etc.
injury	Brain	Boes et al., 2006; Tsitsilonis et al., 2015
	Bone fracture	Gomes and Fernandes, 2011; Haffner-Luntzer et al., 2016; etc.

Table 1 Rodent and fish models in osteoclatogenesis (Continued)

Type	Description	Ref
Transgenic (labeling OCs)	Tg BAC(ctsk:Ctrine)[zf336]	(Apschner et al. 2014)
	Tg (ctsk:YFP)	(Apschner et al. 2014)
	Tg (ctsk:dsred)	(Caetano-Lopes et al., 2020)
	Tg (ctsk:dsred)	(Chatani et al., 2011)
	Tg (Ola.ctsk:EGFP)[zf305]	(Chatani et al., 2011)
	Tg (ctsk: mEGFP)	(To et al., 2012)
	Tg (ctsk: ncGFP)	(To et al., 2015)
	Tg (ctsk:cmcherry)	(To et al., 2012)
	Tg (TRAP:GFP)	(Chatani et al., 2011)
	Tg (trap:GFP-CAAX)[ou2031]	(Kobayashi-Sun et al.,2020)
Transgenic (Osteoporosis)	Tg (rankl:HSE:CFP)	(To et al., 2012)
Mutant (Osteoporosis)	gpr137b (knockout by Crispr/Cas9)	(Urso et al., 2019)
	atp6v1h (knockout by Crispr/Cas9)	(Zhang et al., 2017)
	lgmn (knockout by TALEN)	(Jafari et al., 2017)
	lrp5 (knockdown by morpholino)	(Willems et al., 2015)
	pls3 (knockdown by morpholino)	(van Dijk et al. 2013)
	Gba1 (knockdown by morpholino)	(Zancan et al., 2015)
Physical (Injury)	Skull and jaw	(Geurtzen et al., 2014; Ohgo et al., 2019, etc.)
	Fin rays	(Takeyama et al., 2014; Tomecka et al., 2019; etc.)
	Scales	(Kobayashi-Sun et al., 2020)
(Diet/Drugs)	glucose administration (Type II Diabetes)	(Carnovali et al., 2016)
	dexamethasone	(Huang et al., 2018)
	glucocorticoid-induced osteoporosis	(Pasqualetti et al., 2015; Carnovali et al., 2020)

Chapter 2

Establishment of the zebrafish fractured scale model

1. Introduction

The fish scale, which is a membranous bone that grows out of the skin, has recently attracted great interest in bone research. Scales are protective for the body surface and camouflages through reflection and coloration. When fish scales are lost or damaged, they undergo rapid regeneration through growth and mineralization to restore protective function (Takagi et al., 1989). Fish scales consist of OBs, OCs, and bone matrix as well as epithelial cells and immune cells. A single scale of an adult zebrafish is approximately 2~3 mm in diameter and 20~30 um in thickness. The number of scales depends on the species (e.g. zebrafish have approximately 200 scales), whereas the size of scales is proportional to the body size (Sire et al., 2000). Although the structure of zebrafish scales is quite simple compared with mammalian bones (Han et al., 2018; Chen et al., 2018; Deng et al., 2015), various in vivo and in vitro studies have shown that OCs and OBs in fish scales are influenced by hormones and other substances as those in the mammalian bone (Cappariello et al., 2018; EL Andaloussi et al., 2013; Turchinovich et al., 2019; Gibbings et al., 2009; Tao and Guo, 2019; Huynh et al., 2016; Ikebuchi et al., 2018), indicating that cellular and molecular programs involved in OC and OB regulation are highly conserved among vertebrates. In addition, it is also possible to image OCs and OBs in the scale using fluorescent transgenic lines.

In the present study, a double transgenic zebrafish, *trap:GFP*; *osterix:mCherry*, has been generated to label OCs and OBs with GFP and mCherry, respectively. Tartrate-resistant acid phosphatase (TRAP) is an iron-containing enzyme commonly expressed in OCs and a part of immune cells (Hayman, 2009). There are two splice variants of TRAP proteins in mammals, TRAP5a and 5b. TRAP5a is secreted by macrophages and dendritic cells, whereas TRAP5b is predominantly secreted by OCs. TRAP-deficient mice showed

significantly altered bone morphology with the high density of the bone (Hayman, et al, 1996). Osterix (also known as Sp7) is a zinc finger transcription factor specifically expressed by osteoblasts and plays an essential role in differentiation of osteoblasts (Sinha and Zhou, 2013). Since *trap* and *osterix* are highly expressed in OCs and OBs, respectively, we attempted to visualize and trace OCs and OBs in vivo using scales from *trap:GFP*; *osterix:mCherry* zebrafish.

2. Materials and methods

2.1 Zebrafish husbandry, fracture stimulation, and chemical treatment

Zebrafish were kept in a circulating aquarium system (AQUA) at 28.5°C in a 14/10 h light/dark cycle in accordance with guidelines of the Committee on Animal Experimentation of Kanazawa University. For fracture stimulation, adult zebrafish were anesthetized with 0.01% tricaine (Sigma) in system water. Then, the epidermis area of a scale was cut approximately 400 μm in length under a fluorescent stereomicroscope (Axiozoom V16, Zeiss). For PTH treatment, zebrafish were treated with 10 μM PTH in system water overnight immediately after induction of fracture in scales. The same amount of PBS was utilized as control.

2.2 Generation of transgenic lines

Tg(trap:GFP-CAAX)^{ou2031Tg} and *Tg(osterix:Lifeact-mCherry)^{ou2032Tg}* were generated as previously described[16,17]. A 6 kb and 4.1 kb upstream of the zebrafish *trap* (*acp5a*) gene and the medaka *osterix* (*sp7*) gene were amplified using the primers listed in Table 2, respectively. The amplified products were ligated into pT2AL200R150G vector containing *GFP-CAAX* or *Lifeact-mCherry*. *TPase* mRNA was synthesized from the

pCS2+ vector by in vitro transcription using mMESSAGE mMACHINE SP6 Transcription Kit (Thermo Fisher Scientific). The plasmid construct and *TPase* mRNA were co-injected into 1-cell stage embryos. A stable transgenic line, *Tg(trap:GFP-CAAX)^{ou2031Tg}* and *Tg(osterix:Lifeact-mCherry)^{ou2032Tg}*, was obtained by screening the expression of GFP or mCherry in F1 generation.

2.3 Cell preparation and flow cytometry

Extracted scales were treated with Liberase TM (Roche) in PBS for 1 hour at 37°C. Cells were suspended by pipetting, filtered through 40 μm stainless mesh, and washed twice with 2% fetal bovine serum (FBS) in Hanks' balanced salt solution (HBSS, Wako) by centrifugation (300X g). For staining with Hoechst 33342 (Hoe), cells were resuspended at a density of 10^6 cells/ml in 2% FBS in HBSS and were stained with 5 μg/ml Hoe (Thermo Fisher Scientific) for 90 minutes at 25°C in dark with gentle agitation. Sytox Red (Thermo Fisher Scientific) was added at 5 nM to exclude dead cells or to detect apoptotic cells. Flow cytometric (FCM) acquisition and cell sorting were performed on a FACS Aria III (BD Biosciences). FCM data was analyzed using the Kaluza software (ver. 1.3, Beckman Coulter). The absolute number of cells was calculated by flow cytometry based on acquisition events, times, and the percentage of fractions.

2.4 Intubation anesthesia and imaging

For intubation anesthesia (Fig 2.1), a flask containing 0.05% of 2-phenoxyethanol (Wako) in system water was kept at a constant temperature of 28°C in a water bath. Anesthetic water was delivered to and removed from a glass-bottom chamber (Eppendorf) using peristatic pumps (ATTO). An adult zebrafish mounted in the chamber

was fixed with 0.6% low-gelling agarose (Sigma) and orally perfused with the anesthetic water using a polyethylene tube. For imaging of extracted scales, scales were stained with 5 μg/ml Hoechst 33342 (Hoe) for 20 min at room temperature and mounted in a glass bottom dish (Matsunami) containing 0.6% low-gelling agarose. Fluorescent images were captured using an FV10i confocal microscope and Fluoview FV10i-SW software (ver. 2.1.1) (Olympus). For time-lapse imaging, images were captured every 5 min and movies were generated using iMovie software (ver. 10.1.12). The intensity more than 4-fold higher than the average intensity of GFP$^+$ cells in the intact scale and more than 10-fold higher than the average intensity of mCherry in the whole intact scale were defined as GFP^{bright} and mCherry^{bright}, respectively.

2.5 Electron microscopy

Sorted cells were fixed with 2.5% glutaraldehyde (Nacalai Tesque), 2% paraformaldehyde (Wako) in 0.1 M phosphate buffer (pH 7.4) at 4 °C overnight. Cells were dehydrated and embedded in Epon 812 (TAAB Laboratories). Ultrathin sections were obtained from the Epon blocks and stained with uranyl acetate and lead citrate. Sections were observed by transmission electron microscopy (H-7650, Hitachi).

2.6 Statistical analysis

Unpaired two-tailed Student's t-test or one-way ANOVA with Dunnett's test was used to determine statistical differences between groups. A value of $p < 0.05$ was considered to be statistically significant.

3. Results

3.1 Convergence and fusion of OCs in the fractured scale

To examine spatial distribution of OCs and OBs in the scale, confocal imaging of extracted scales was performed. In an intact scale, *osterix:mCherry*^{+} cells were entirely distributed in the scale including the epidermis and dermis area, while *osterix:mCherry*^{bright} cells were predominantly observed at the edge region of the scale. In contrast, only a few *trap:GFP*^{+} cells were observed in the scale (Fig. 2.2a). These *trap:GFP*^{+} cells mostly showed a small and round morphology. To induce fracture stress, the epidermis area of the scale was cut approximately 400 μm in length and confocal imaging was performed at 2 days post-fracture (d.p.fr.). Interestingly, the fracture site was covered with many *trap:GFP*^{bright} cells having more than ten nuclei (Fig. 2.2b), indicating that multinucleated OCs are formed and converged in the fracture site.

To examine the fracture healing process in the scale, in vivo imaging was performed using an intubation anesthesia system (Fig. 2.1). At 1 d.p.fr., many small round *trap:GFP*^{+} cells were detected around the edge region close to the fracture site where *osterix:mCherry*^{bright} cells are abundantly distributed (Fig. 2.2c). These *trap:GFP*^{+} cells seemed to interact with *osterix:mCherry*^{bright} cells. At 2 d.p.fr., although *trap:GFP*^{+} cells in the edge region decreased, a number of *trap:GFP*^{bright} cells covered the fracture site. These data suggest that OCs interact with OBs mainly in the edge region of the scale before reaching the fracture site. After 4 d.p.fr., the number of *trap:GFP*^{+} cells decreased, and the fracture site was covered with *osterix:mCherry*^{+} cells instead, leading to bone formation by OBs. To trace *trap:GFP*^{+} cells in the fractured scale, time-lapse imaging was performed in *trap:GFP* animals at 1 d.p.fr. Small *trap:GFP*^{+} cells actively migrated and fused to generate multinucleated OCs around the fracture site. After fusion, cells were

larger in size and brighter in GFP expression compared to unfused cells (Fig2.3a and 2.3b). Collectively, these data indicate that the transgenic lines, *trap:GFP* and *osterix:mCherry*, finely label OCs and OBs, respectively, and that the fractured scale is a useful model to investigate the process of OC differentiation in vivo.

3.2 Variation of OCs and OBs in the fractured scale

To further characterize OCs and OBs in the scale, cells were harvested from scales in double-transgenic animals and analyzed by flow cytometry (FCM). When living cells were displayed in a GFP vs. mCherry plot, *trap:GFP*$^+$ cells and *osterix:mCherry*$^+$ cells were detected in both intact and fractured scales at 1 d.p.fr. Unexpectedly, however, most *trap:GFP*$^+$ cells were within the *osterix:mCherry*$^+$ fraction in the scale (Fig. 2.4a). Compared with intact scales, the percentage of *trap:GFP*^{low} *osterix:mCherry*$^+$ ("GFP^{low}") and *trap:GFP*^{high} ("GFP^{high}") cells in fractured scales significantly increased (Fig. 2.4b). Approximately 75% of *trap:GFP*^{high} cells were detected in the mCherry$^+$ fraction in fractured scales (Fig 2.4c). Cells in the scale were subdivided into three fractions, *trap:GFP*$^-$ *osterix:mCherry*$^+$ ("mCh$^+$"), GFP^{low}, and GFP^{high} cells, and the absolute number of these three fractions was examined in intact or fractured scales. Compared with intact scales, the number of GFP^{low} and GFP^{high} cells in fractured scales at 1 d.p.fr. was approximately 2.1 and 3.7 times higher, respectively, whereas that of mCh$^+$ cells was unchanged (Fig. 2.4d).

Cells within the mCh$^+$, GFP^{low}, and GFP^{high} fraction at 1 d.p.fr. were separately sorted and morphologically examined on a fibronectin-coated glass-bottom dish by confocal microscopy. mCh$^+$ cells contained at least three different types of OBs: small and round cells (type-1), small and spindle shaped cells (type-2), and large and highly

spread cells (type-3). Approximately 60% of mCh$^+$ cells were type-1 in the fractured scale. Cells in the GFP^{low} fraction were small and round mononucleated (type-1), whereas a part of GFP^{low} cells did not express GFP, but did contained GFP$^+$ fragments in the cytoplasm, which seem to be a phagocyte-like cell (type-2) or an mCh$^+$ OB (type-3) (Fig. 2.5a). In contrast, cells in the GFP^{high} fraction contained a few different types of OCs. Some showed a small and round morphology containing a single nucleus (type-1), whereas some displayed an amoeba-like morphology with many pseudopodia and single or two nuclei (type-2). A few GFP^{high} cells contained three to four nuclei and showed larger cell size (type-3), suggesting that various stages of OCs may be present in the GFP^{high} fraction (Fig. 2.5c). It should be noted that type-2 OCs actively migrated on a fibronectin-coated dish, whereas type-1 and type-3 OCs showed low motility. Interestingly, *trap:GFP$^+$* cells mostly had mCherry$^+$ particles in the cytoplasm (Fig. 2.5b, c). Ultrastructural analysis revealed that GFP^{high} cells possessed small protrusions, irregular shaped nuclei, abundant mitochondria, and compact Golgi apparatus located near the nucleus (Fig. 2.5d), which are typical morphological features of OCs (Baron et al., 1986). Various types of vesicles, including secondary lysosomes, early endosomes, and multi-vesicular bodies, were also observed in the cytoplasm of GFP^{high} cells (Fig. 2.5d).

3.3 PTH treatment enhanced OB and OC activity

Intermittent low-dose recombinant human PTH promotes bone healing by upregulating Runx2 expression in OBs at the early stage of fracture healing (Tsuchie et al., 2013; Ban et al., 2019). To examine the effect of PTH on the activity of OBs and OCs, zebrafish were treated with 10 μM PTH overnight immediately upon the induction of fracture in scales. Time-lapse imaging analysis revealed that a relatively higher number of mCherry$^+$

OBs migrated and converged at the fracture site at 1 d.p.fr. in PTH-treated zebrafish compared with PBS-treated control zebrafish (Fig 2.7a). FCM analysis also showed that the percentage of mCh$^+$ OBs and GFP^{high} OCs were both significantly increased in PTH-treated zebrafish (Fig 2.7b), suggesting that both OBs and OCs are activated by PTH treatment, as has been shown in mammals (Tsuchie et al., 2013; Ban et al., 2019).

4. Discussion

In zebrafish, mononucleated and multinucleated OCs have been shown to be present in embryonic stage to adulthood (Sharif et al., 2014). Multinucleated OCs in zebrafish display similar features to those in mammals, e.g., formation of Howship's lacnae and positive for TRAP (Witten et al., 2001). In the present study, a fracture healing model has been established using the scale of *trap:GFP*; *osterix:mCherry* double-transgenic zebrafish, and this model allow us to visualize and trace OCs and OBs during fracture healing. Unlike analyses in mammalian models, the whole process of fracture healing can be monitored using zebrafish scales. During the healing process, fusion of mononuclear OCs was successfully captured by live-imaging analysis of the scale. Moreover, it is also possible to isolate *trap:GFP$^+$* OCs and *osterix:mCherry$^+$* OBs from the scale, enabling to examine the morphology and expression of genes of interest.

Cells within the mCh$^+$ fraction contained at least three different types of OBs according to their morphology. During scale regeneration, highly activated OBs increase and become larger compared to ontogenetic scales (Yoshikubo et al., 2015). Iwasaki et al. showed that zebrafish scales contain three distinct types of OBs due to their different location and size (Iwasaki et al., 2018). Since there are no antibodies or marker genes available to distinguish the subpopulation of OBs, future works are needed to examine

the activity and function of these different types of OBs in the fractured scale.

Cells within the GFP^{high} fraction also contained several subpopulations with different morphology. In mice, mature OCs undergo a transition between two distinct states based on the motility and function, bone-resorptive 'R-type' and moving non-resorptive 'N-type' (Kikuta et al., 2013). Takeyama et al. established a fracture healing model using the fin ray of medaka and found that two different types of OCs were induced before and after OB callus formation (Takeyama et al, 2014). Early-induced OCs are small in size with low TRAP activity, and show no clear zone, while the late ones show larger in size with high TRAP activity and possess clear zone. Both types of OCs show no ruffled border and appeared near but not on the fractured site or the callus. It is still unclear, however, how these two types of OCs are generated and activated in the bone tissue.

As mentioned in Chapter 1, although fin ray is also an attractive organ to visualize OCs and OBs due to the transparency and thickness of the tissue, it is difficult to quantify the number of OCs and OBs and monitor the process of fracture healing in the entire fin because of the large size of the tissue. In contrast, the scale is a tiny tissue and each scale is separated on the surface of the body, enabling to trace OCs and OBs in the entire bone tissue in the scale. Thus, the zebrafish scale has some unique advantages for the study of OCs and OBs.

Although parathyroid glands are developed from the amphibian in vertebrates, the PTH gene has been discovered in teleosts including zebrafish. Zebrafish have two PTH genes, zPTH1 and zPHT2. zPTH1 protein were detected in the neuromasts of the lateral line and the central nervous system during embryogenesis (Hogan et al., 2005), suggesting that PTH is synthesized in the neutral tissues and plays an important physiological role in teleosts. Suzuki et al. found that treatment of goldfish scales with PTH1 resulted in the

activation of OBs and OCs in vitro (Suzuki et al., 2011). In mice, intermittent administration of PTH for more than 3 weeks increases the frequency of physical interaction between OBs and OCs, leading to increased bone volume without enhancing bone resorption (Furuya et al., 2018). Consistent with this observation, the percentage and absolute number of mCh[+] OBs and GFP[high] OCs significantly increased in the fracture scales from PTH-treated zebrafish compared with controls, indicating that OBs and OCs in zebrafish scales respond to PTH treatment as they do in mammals. These data highlights that the zebrafish scale model can also be applied to screen candidates of drug/chemical compounds for regulation of OCs and OBs.
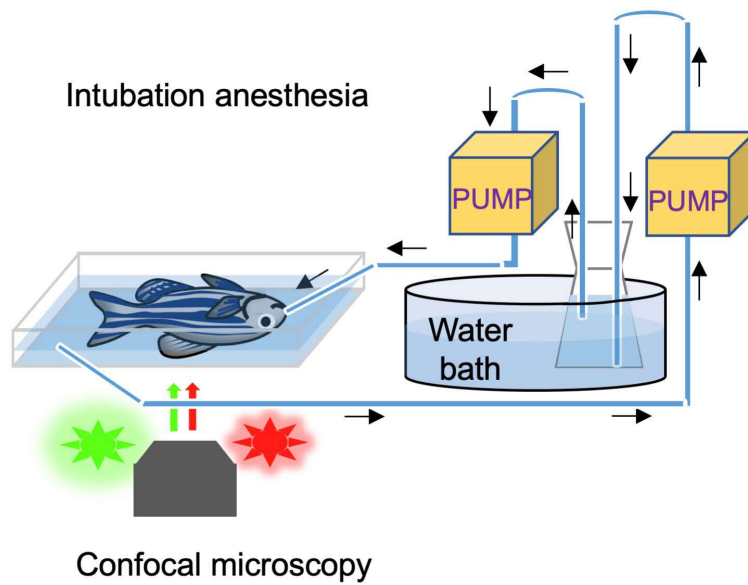
Figure 2.1 Intubation anesthesia system.

A flask containing 2-phenoxyethanol (2-PE) in system water is maintained in a water bath to keep a constant temperature of 28°C, and delivered to a glass-bottom chamber by a peristatic pump. A transgenic zebrafish mounted in the chamber is orally perfused with the anesthetic water in order to image scales by confocal microscopy.
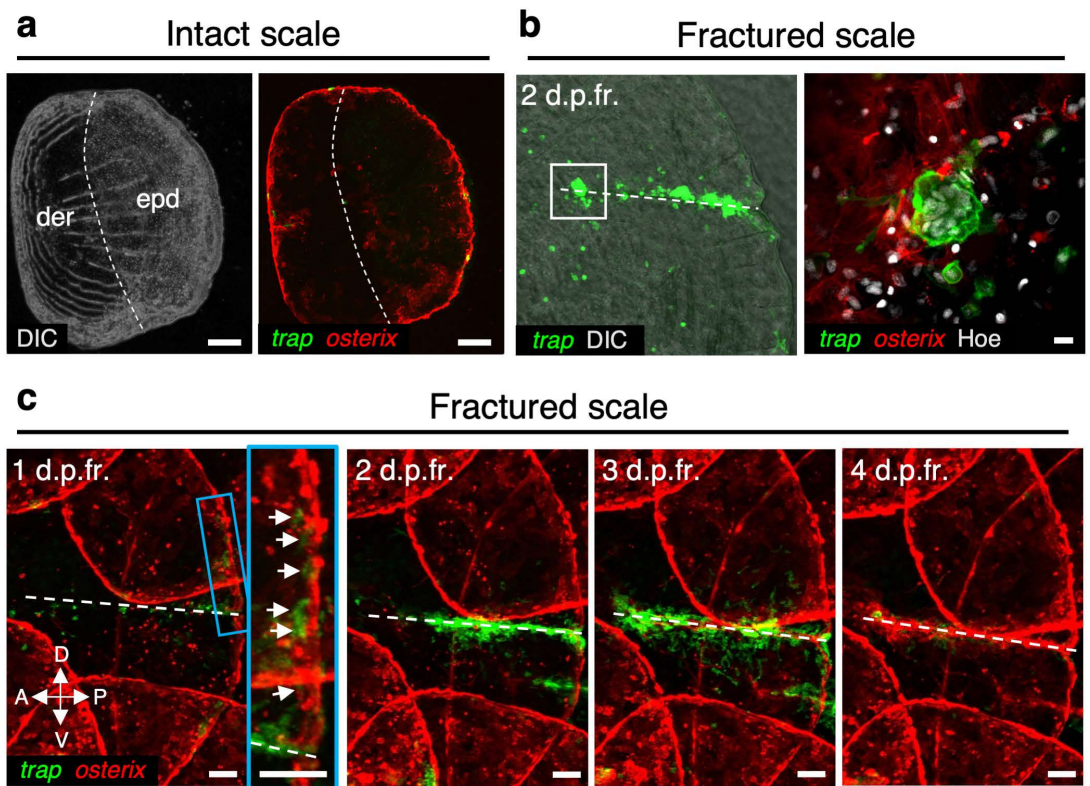
Figure 2.2 *trap:GFP⁺* **cells converge at the fracture site in the scale.**

(**a**, **b**) Representative images of an intact (**a**) or fractured scale (**b**) of *trap:GFP*; *osterix:mCherry* double-transgenic zebrafish. Dotted lines in **a** show a boundary of the dermis (der) and epidermis (epd) area. The right panel in **b** shows a high magnification image of the white boxed area in the left panel. (**c**) Time-course changes of a fractured scale. The inset in the left panel shows a high magnification image of the blue boxed area. Images are orientated with the anterior side to the left and the dorsal side to the top. Arrows indicate *trap:GFP⁺* cells detected in the edge region of the fractured scale. Dotted lines in **b** and **c** show the fracture site. DIC, differential interference contrast; Hoe, Hoechst 33342; d.p.fr., days post-fracture; bars, 200 μm (**a**); 10 μm (**b**); 100 μm (**c**).
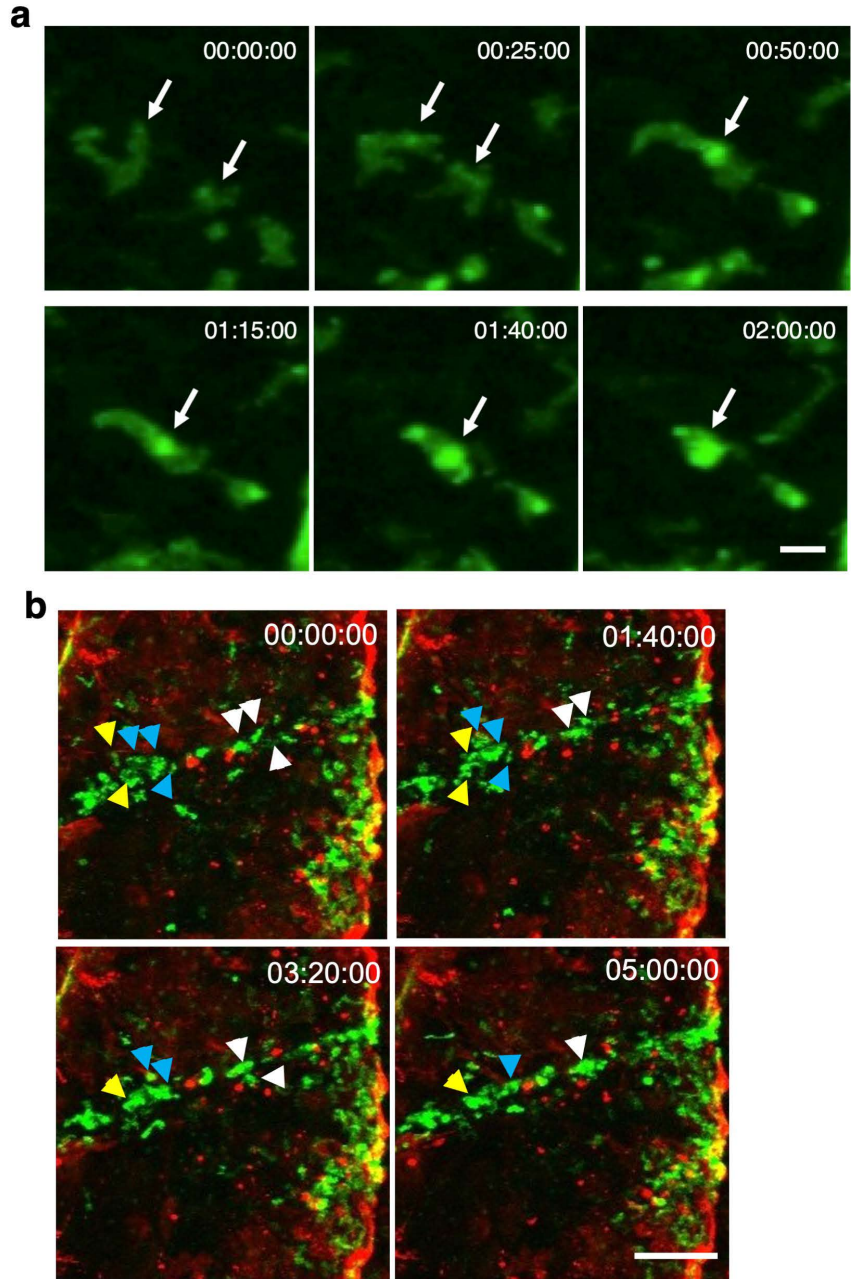
Fig 2.3 *trap:GFP*+ OCs fuse near the fracture site.

(**a**) Fusion of GFP+ OCs in the fractured scale. (**b**) Time-lapse imaging of a fractured scale in a *trap:GFP*; *osterix:mCherry* double-transgenic zebrafish at 1.5 d.p.fr. Arrows indicate a *trap:GFP*+ OC that will fuse to become a GFP[bright] OC near the fracture site. Bars, 20 μm (**a**), 100 μm (**b**).
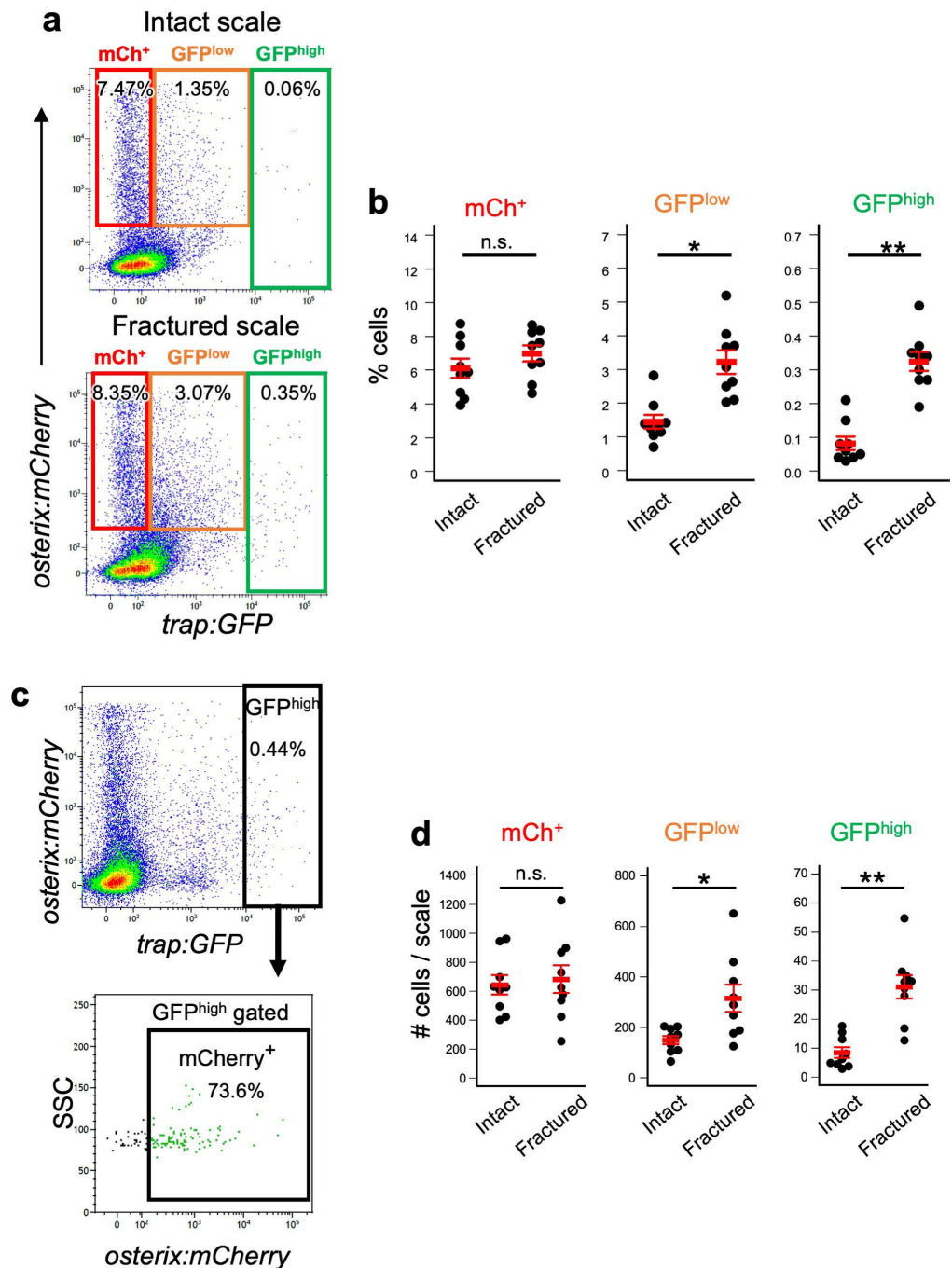
Figure 2.4 The number of OCs increases in the fractured scale.

(**a**) Representative results of FCM analysis of cells from intact (upper panel) or fractured scales at 1 d.p.fr. (lower panel). Red, orange, and green gate show *trap:GFP⁻ osterix:mCherry⁺* (mCh⁺), *trap:GFP*^{low} *osterix:mCherry⁺* (GFP^{low}), and *trap:GFP*^{high} (GFP^{high}) cells, respectively. (**b**) The percentage of mCh⁺, GFP^{low}, and GFP^{high} cells in intact or fractured scales at 1 d.p.fr. (**c**) Representative results of FCM analysis of cells in scales at 1 d.p.fr. from *trap:GFP*; *osterix:mCherry* double-transgenic animals. GFP^{high} cells in the upper panel are displayed in an *osterix:mCherry* vs. side scatter (SSC) plot (lower panel). (**d**) Absolute number of mCh⁺, GFP^{low}, and GFP^{high} cells per an intact or fractured scale at 1 d.p.fr. Error bars, s.e.m (n = 9 for each group); n.s., no significance; *$p < 0.05$; **$p < 0.001$ by Student's *t*-test.

Figure 2.5 Different types of OBs and OCs from the fractured scale

(**a-c**) Images of mCh+ (**a**), GFPlow (**b**), and GFPhigh cells (**c**). Arrows indicate an mCherry+ particle detected in the cytoplasm. Numbers in bottom left of each panel indicate the number of cells showing the displayed morphology over the total number of observed cells. DIC, differential interference contrast. (**d**) Ultrastructure of a GFPhigh cell. Arrowheads show vesicles, which include secondary lysosomes, multi-vesicular bodies, and early endosomes. n, nucleus; m, mitochondrion; g, Golgi apparatus; bars, 5 μm (**a-c**); 1 μm (**d**).

Figure 2.6 PTH treatment enhances the activation and differentiation of OBs and OCs.

(**a**) *osterix:mCherry*⁺ OBs converged at the fracture site from 3 to 6.4 hours post-fracture. Images were captured every 5 min. Numbered arrows indicate a migrating OB. (**b**) The percentage of mCh⁺, GFP^low, and GFP^high cells in the intact scale or fractured scale of PBS- or PTH-treated zebrafish. Bar, 100 μm. *$p < 0.05$ by Student's *t*-test.

Chapter 3

Uptake of OB-derived EVs facilitates OC differentiation in the zebrafish scale

1. Introduction

The integrity of bone tissue is maintained by a fine balance between the activity of OBs and OCs, ensuring no net change in bone mass (Amaresekar et al., 2018). OCs are differentiated from hematopoietic stem cells and become a multinucleated cell by cell fusion, and it can resorb bone via secretion of hydrochloric acid (Chatani et al., 2011; Renn et al., 2006). In contrast, OBs are differentiated from mesenchymal stem cells and can produce bone matrix, such as type I collagen (Sire et al., 1990). Differentiation and activity of OCs were regulated by OBs via signaling molecules (de Vrieze et al., 2011), highlighting the importance of cell communication between these two types of cells in osteoclastogenesis.

There are two well-known modes of OB – OC interaction. The first is a direct contact between OBs and OC precursors based on interaction of membrane-bound ligands and receptors to initiate intercellular signaling (e.g. RANKL (Receptor activator of nuclear factor kappa B ligand)-RANK signaling). The second is based on diffusible paracrine factors secreted by OBs, which act on OC precursors (e.g. M-CSF (Macrophage-colony stimulating factor)) (Pasqualetti et al., 2012; Suzuki et al., 2000; Suzuki et al., 2002). In addition, recent studies provide evidence that OB-derived extracellular vesicles (EVs) can be considered a third mode of OB – OC interaction. EVs transfer proteins, lipids, and RNAs between various cell types (Witten et al., 2017; Raggatt et al., 2010). Molecular composition of EVs is dependend on the releasing cell type and the external stimuli to the cell (Carnovali et al., 2016; Park et al., 2016). However, hitherto only a few studies have showed that EVs are involved in interaction between OBs and OCs. Microvesicles (MVs, one type of EVs) shed from an OB cell line, UAMS-32P, contain RANKL proteins and can transfer signals to OC precursors through a cell-

surface receptor RANK, leading to differentiation of OCs in vitro (Deng et al., 2015). Inhibition of EVs in UAMS-32P cells by imipramine can prevent ovariectomy-induced bone loss (Deng et al., 2017). A proteomics study on EVs derived from a murine OB cell line, MC3T3, demonstrated that many proteins enriched in EVs are involved in integrin signaling, mammalian target of rapamycin (mTOR) signaling, and eukaryotic inhibition factor 2 (EIF2) signaling (Ge et al., 2015), which are essential for bone remodeling and fracture healing. Cappariello et al. showed that EVs obtained from cultured primary OBs can contribute to the pro-osteoclastic effect in a RANKL-dependent manner (Cappariello et al., 2018). On the other hand, it is also reported that OC-derived EVs promote OB differentiation, whereas they inhibit osteoclastogenesis (Ikebuchi et al., 2018, Huynh et al., 2016). Mature OC-derived apoptotic bodies (ABs, one type of EVs) can also promote OB differentiation via RANK-mediated reverse signaling in vitro (Ma et al., 2019). It is still unknown, however, if OC precursors actually engulf OB-derived EVs in vivo to promote their differentiation due to the difficulty of live-imaging in the bone tissue.

As shown in Chapter 2, flow cytometric analysis of fractured scales from a double-transgenic animal, *trap:GFP*; *osterix:mCherry*, revealed that most *trap:GFP*high OCs at 1 d.p.fr. were detected in the mCherry+ fraction. In addition, morphological analysis showed that *trap:GFP*high OCs contain mCherry+ particles in their cytoplasm. It is still unclear, however, how OCs obtain mCherry+ particles and what roles these particles play in OCs. Therefore, the studies in Chapter 3 are intended to characterize OB-derived EVs by live-imaging, electron microscopy, RNA-seq, and cell culture assays.

2. Materials and Methods

2.1 Fish husbandry and fracture stimulation

Fish were kept as described in Chapter 2 (Materials and Methods 2.1).

2.2 Cell preparation and flow cytometry

Cells were harvested from scales as described in Chapter 2 (Materials and Methods 2.3). For staining with Hoechst 33342 (Hoe), cells were suspended at 10^6 cells/ml in 2% FBS in HBSS and were stained with 5 μg/ml Hoe (Thermo Fisher Scientific) for 90 min at room temperature with gentle agitation. For staining with Annexin-V, cells were washed with Cell Staining Buffer (BioLegend) by centrifugation (1,600 rpm, 7 min, 4°C), followed by staining with Annexin-V-FITC in Annexin-V binding buffer (BioLegend) for 15 min at room temperature. FCM analysis, sorting, and data analysis were performed as described in Chapter 2 (Materials and Methods 2.3). The detectable size of cells/particles by FACS Aria III is more than 0.5 μm, indicating that only large EVs (> 0.4 μm) can be isolated in this analysis. To isolate EVs from scales, therefore, samples were prepared according to the same procedure with cells described above without high-speed centrifugation.

2.3 Preparation of kidney marrow cells

Kidney marrow cells (KMCs) were obtained by pipetting of a dissected kidney in 1 mL of ice-cold 2% FBS in HBSS and centrifuged as described above. To lyse erythrocytes by osmotic shock, the cell pellet was gently mixed with 1 mL of ultrapure water by pipetting. Subsequently, 1 mL of 2X HBSS was added. Cells were then filtered through a 40 μm stainless mesh and washed twice with 2% FBS in HBSS by centrifugation.

2.4 Confocal imaging

Fluorescent images were captured by confocal microscopy as described in Chapter 2 (Materials and Methods 2.4).

2.5 Cell culture

Approximately 6×10^4 KMCs from *trap:GFP* animals were suspended in 8% FBS, 32% Dulbecco's modified Eagle's medium (Wako), 40% Leiboviz's L-15 medium (Wako), and 12% Ham's F12 medium (Wako) supplemented with 2mM L-glutamine (Wako), 15mM 4-(2-hydroxyethyl)-1-piperazineethanesulfonic acid (HEPES, Sigma), and 100U penicillin (Wako), and 100 μg/mL streptomycin (Wako). KMCs were then plated on a 96-well plate coated with fibronectin (Corning) and incubated for 3 hrs at 30°C, 5% CO_2. Subsequently, approximately 2,000 EVs or sorted cells were plated and incubated for additional 2 days at the same condition. Hoe was directly added into the medium at the concentration of 5 μg/ml to count the number of nuclei. The number of GFP^+ cells and nuclei was counted using an EVOS FL Cell Imaging System (Thermo Fisher Scientific). For counting the total number of cells in each well, cells were treated with 0.25% trypsin - 1mM EDTA, collected by pipetting, and counted using a hemocytometer (Funakoshi).

2.6 RNA-seq and qPCR

Total RNAs wete extracted using RNeasy Mini Kit. Reverse transcription (RT) was performed using Super Script III (Thermo Fisher Scientific) and an RT primer listed in Table 2. RT primers were then digested by exonuclease I (Takara), and a poly-A tail was added to the 3' ends of the first-strand cDNAs using terminal transferase (Sigma). The

second-strand DNA was synthesized using MightyAmp DNA polymerase (Thermo Fisher Scientific) and a tagging primer listed in Table 2. PCR amplification was performed using a suppression primer listed in Table 2. Amplified double-strand cDNAs wete purified using QIAquick PCR Purification Kit (Qiagen). RNA-seq library was prepared using Nextera XT DNA Library Preparation Kit (illumina). Next generation sequencing was performed by GENEWIZ using the Illumina NextSeq500 (illumina), and base-calling was performed using the Illumina RTA software (ver. 2.4.11). Sequence reads were mapped to the zebrafish reference genome (GRCz11) using HiSAT2 (version 2.1.0). Tags per million (TPM) were calculated using Subread (ver. 1.6.4). Differentially expressed genes were selected with a p-value cutoff of 0.05 based on one-way ANOVA and more than 2-fold change. Principal component analysis (PCA) and hierarchical clustering were performed in R (ver. 3.5.0) with the Bioconductor gplots package. The expression data have been uploaded to the Gene Expression Omnibus (GEO) database (National Center for Biotechnology Information) and the accession number is GSE134330. Total RNAs from the adult fin were extracted as described above and cDNAs were synthesized with ReverTra Ace qPCR RT Master Mix (Toyobo). Quantitative PCR (qPCR) assays were performed using TB Green Premix Ex Taq II (TaKaRa) on a ViiA 7 Real-Time PCR System according to manufacturer's instructions (Thermo Fisher Scientific). Primers used for qPCR are listed in Table 2.

2.7 Electron microscopy

For negative staining, a grid with a supporting film was placed on a drop of the EV suspension for 15 minutes, followed by being placed in 2% uranium acetate aqueous solution for 2 minutes. After air-drying, EVs were captured under an electron microscope

(H-7650, Hitachi).

2.8 X-ray irradiation and transplantation

Six zebrafish were placed in a 90 mm petri dish filled with system water, and animals were irradiated with X-ray on a Faxitron RX-650 (Faxitron, 130 kVp, 1.15 Gy/min) for 20 min (approximately 23 Gy). At 2 days post-irradiation, animals were transplanted with approximately 2 X 10^5 KMCs using a retro-orbital injection method.

2.9 Statistical analysis

Statistical analysis was performed as described in Chapter 2 (Materials and Methods 2.6).

3. Results

3.1 Transplantation assays confirm uptake of OB-derived EVs in OCs

Since the majority of *trap:GFP*^{+} cells possessed mCherry[+] particles (Fig 2.5), it is likely that OC precursors engulf OB-derived EVs to become mature OCs under fracture stress. OCs are derived from hematopoietic stem cells, while OBs are derived from mesenchymal stem cells (Udagawa et al., 1990, Rutkovskiy et al., 2016), indicating that transplantation of hematopoietic stem cells is useful to determine if donor-derived OCs can obtain OB-derived particles in the recipient scale. First, KMCs including hematopoietic stem cells (Traver et al., 2003; Kobayashi et al., 2014; Kobayashi et al., 2019) were collected from *trap:GFP*; *osterix:mCherry* double-transgenic animals and transplanted into sublethally irradiated wild type recipients. After 20 weeks post-transplantation, scales in recipients were fractured and analyzed by FCM or confocal

microscopy at 1 d.p.fr. (Fig. 3.1a, "Transplantation-1"). Only *trap:GFP* single-positive cells, but not *osterix:mCherry*-expressing cells, were detected in the recipient scales (Fig. 3.1b, c; n = 3), indicating that *trap:GFP*[+] OCs originate from hematopoietic stem cells in zebrafish, as has been shown in mammals (ref). Besides, the possibility of ectopic mCherry expression in OCs was eliminated. Second, KMCs from *trap:GFP* single-transgenic animals were transplanted into sublethally irradiated *osterix:mCherry* single-transgenic recipients (Fig. 3.1a, "Transplantation-2"). In this case, GFP and mCherry double-positive cells were detected in the fractured recipient scale. The percentage of mCherry^{+} cells within the *trap:GFP*[high] fraction was 48.1 ± 13.5% (n = 4, ± s.d.) in recipient scales (Fig. 3.1b).

Supporting these transplantation assays, live-imaging analysis of OBs and OCs in the fractured scale of double-transgenic animals showed that a *trap:GFP*[+] OC interacted with *osterix:mCherry*[+] OBs and obtained mCherry[+] particles before reaching the fracture site (Fig 3.2a). Interestingly, a *trap:GFP*[+] cell had a protrusion and extended it toward mCherry[+] particles to engulf them into the cytoplasm (Fig. 3.2a, b). Taken together, these data suggest that *trap:GFP*[+] OCs engulf OB-derived EVs in the fractured scale.

3.2 OB-derived EVs contain signaling molecules

In order to characterize OB-derived EVs in the scale, the next study is intended to isolate OB-derived EVs from fractured scales using Hoechst 33342 (Hoe), a DNA fluorescent dye for living cells. FCM analysis of 1 d.p.fr. fractured scales showed that the *osterix:mCherry*[+] fraction was subdivided into two fractions based on Hoe staining, Hoe[high] and Hoe[low]. An mCh[+] Hoe[low] fraction contains non-nucleated *osterix:mCherry*[+] particles with very low forward scatter (FSC) intensity (Fig. 3.3a, b). Electron

microscopic analysis revealed that the majority of mCh$^+$ Hoe^{low} particles were $0.6 - 1.0$ μm in diameter, although a part of particles were more than 2 μm (Fig. 3.3b, c). The number of mCh$^+$ Hoe^{low} particles increased approximately three times in the fractured scale compared with the intact scale, suggesting that fracture stress stimulates release of OB-derived EVs (Fig. 3.3d).

To analyze transcriptome in OCs, OBs, and OB-derived EVs, RNA-seq analysis was performed on four different populations in the fractured scale at 1 dpf: GFP$^-$ mCh$^+$ Hoe^{high} ("mCh$^+$" fraction), GFP^{low} mCh$^+$ Hoe^{high} ("GFP^{low}" fraction), GFP^{high} Hoe^{high} ("GFP^{high}" fraction), and mCh$^+$ Hoe^{low} ("EV" fraction) (Fig. 3.4a). Principal component analysis (PCA) showed that expression patterns in mCh$^+$ and EV were far, whereas those in GFP^{low} and GFP^{high} were very close (Fig. 3.4b). OC-related genes, such as *ctsk* (*cathepsin K*), *nfatc1* (*nuclear factor of activated T cells 1*), *csk* (*C-terminal Src kinase*), *mmp9* (*matrix metallopeptidase 9*), *itgb3b* (*integrin beta 3b*), and *atp6v* (*ATPase, H+ transporting V*) family genes, were highly expressed in the GFP^{high} fraction (Fig. 3.4c). In contrast, OB-related genes, such as *col1a1a* (*collagen, type I, alpha 1a*), *alpl* (*alkaline phosphatase, biomineralization associated*), *runx2b* (*RUNX family transcription factor 2b*), *efnb2a* (*ephrin-B2a*), *csf1a* (*colony stimulating factor 1a*), *wnt10b* (*wingless-type MMTV integration site family, member 10b*), and *tgfb1a* (*transforming growth factor, beta 1a*), were predominantly expressed in the mCh$^+$ fraction (Fig. 3.4d).

To further examine the expression pattern of each fraction, up-regulated genes were selected in each fraction and gene ontology enrichment analysis was performed in each gene set. Genes involved in "ATP metabolic process" and "proton transmembrane transport" were highly expressed in the GFP^{high} fraction, indicating that OCs are present in the GFP^{high} fraction. In contrast, genes involved in "immune system process" and

"leukocyte activation" were highly expressed in the GFP^{low} fraction (Fig. 3.4e). In combination with morphological analysis and expression data, it is likely that cells in the GFP^{low} fraction mainly contain monocytes/macrophages, which are known to be the precursors of OCs (Baron et al., 1986; Udagawa et al, 1990; Boyce, 2013). Genes involved in "response to wounding" and "extracellular matrix organization" were predominantly expressed in the mCh$^+$ fraction. In contrast, genes involved in "intracellular signal transduction", "vesicle-mediated transport", and "phagocytosis" were enriched in the EV fraction (Fig. 3.4e), raising the possibility that OB-derived EVs abundantly contain signaling molecules.

Quantitative PCR analysis also revealed that OC-related genes, *trap*, *ctsk*, and *nfatc1*, were predominantly expressed in the GFP^{high} fraction, whereas OB-related genes, *osterix*, *col1a1*, *alpl*, and *osteocalcin* (also known as *bone gamma-carboxyglutamate protein* (*bglap*)) were highly expressed in the mCh$^+$ fraction (Fig. 3.5). In mammals, OC precursors and OBs express RANK and RANKL on the surface of their plasma membrane, respectively. RANKL-RANK signaling activates some downstream signaling pathways that are involved in OC differentiation (Kikuta et al., 2013; Ikubuchi et al., 2018). Both *rank* and *rankl* were highly expressed in both the GFP^{low} and EV fraction in the fractured scale (Fig. 3.5), suggesting that differentiation of OCs can be induced by OB-derived EVs.

3.3 OB-derived EVs promote OC differentiation via Rankl signaling

According to their sizes and origins, EVs are classified into three types: exosomes, MVs, and ABs (EL Andaloussi et al., 2013 ; van Niel et al., 2018). Exosomes and MVs are released by a variety of cell types and involved in cell-cell communication (Deng et al., 2015; Cappariello et al., 2018; Tao and Guo, 2019). ABs are formed in the process of

apoptosis and engulfed by macrophages or other immune cells (Budai et al., 2019). Because exosomes are classified as very tiny vesicles (< 100 nm) (EL Andaloussi et al., 2013), OB-derived EVs isolated by FCM and visualized by confocal microscopy can be classified as MVs and/or ABs. To separate MVs and ABs, Sytox Red and Annexin-V were utilized, which can distinguish live, pre-apoptotic, and apoptotic cells as well as MVs and ABs (Wlodkowic et al., 2009). FCM analysis revealed that mCh$^+$ Hoe^{high} OBs were divided into three fractions, Sytox Red^{low} Annexin V^{low} (live cell fraction; 79.2 ± 2.4%), Sytox Red^{low} Annexin V^{high} (pre-apoptotic cell fraction; 7.1 ± 1.3%), and Sytox Red^{high} Annexin V^{high} (apoptotic cell fraction; 11.2 ± 1.0%). In the mCh$^+$ Hoe^{low} EV fraction, the percentage of Sytox Red^{low} Annexin-V^{low} "MV" fraction was 65.4 ± 5.0%, while that of Sytox Red^{low} Annexin-V^{high} "AB" fraction was 32.2 ± 5.9% (n = 4, ± s.d.) (Fig. 3.6a, b), suggesting that both MVs and ABs are in mCh$^+$ Hoe^{low} EVs in the fractured scale.

To examine the role of OB-derived EVs in OC differentiation, 60,000 KMCs from *trap:GFP* animals were co-cultured with 2,000 OBs (mCh$^+$ Hoe^{high} Sytox Red^{low} Annexin-V^{low}), MVs (mCh$^+$ Hoe^{low} Sytox Red^{low} Annexin-V^{low}), or ABs (mCh$^+$ Hoe^{low} Sytox Red^{low} Annexin-V^{high}) on a fibronectin-coated plate. At 2 days of culture, the number of *trap:GFP$^+$* cells significantly increased in cells co-cultured with MVs or OBs compared to non-co-cultured controls. Moreover, the number of *trap:GFP$^+$* cells also significantly increased in cells co-cultured with ABs (Fig. 3.6c, d). Similar with OCs in the fractured scale (shown in Fig. 2.5c), mCherry$^+$ particles were detected in the cytoplasm of *trap:GFP$^+$* cells co-cultured with OBs, MVs, or ABs (Fig. 3.6e).

To better understand the role of OB-derived EVs, KMCs were cultured with or without OB-derived EVs (mCh$^+$ Hoe^{low}). Treatment of OB-derived EVs results in the increased number of *trap:GFP$^+$* cells, whereas the total number of KMCs was unchanged (Fig. 3.7a,

b), suggesting that EVs do not affect proliferation of hematopoietic cells, but do affect OC differentiation. Furthermore, treatment of EV significantly increased the frequency of multinucleated *trap:GFP*^{+} cells. A few *trap:GFP*^{+} cells possessed more than three nuclei after treatment with OB-derived EVs (Fig. 3.7c). Collectively, these data suggest that differentiation and fusion of OCs are promoted by treatment of OB-derived EVs in vitro.

Because *rankl* was highly detected in OB-derived EVs, the next study is intended to determine if OB-derived EVs promote OC differentiation by mediating Rankl signals. A gene knockdown method based on the CRISPR/Cas9 system was utilized, in which injection of four guide RNAs (gRNAs) targeting the gene of interest recapitulates mutant phenotypes (Wu et al., 2018). Cas9 proteins were co-injected with four gRNAs targeting either exon 1 or 4 of *rankl* gene into one-cell stage embryos from *trap:GFP; osterix:mCherry* zebrafish (Fig. 3.8a). Although animals injected with *rankl* gRNA partially survived into adulthood, most adults displayed severe body curvature (Fig. 3.8b). qPCR analysis using two different sets of primers that recognize gRNA target sites of *rankl* gene confirmed approximately 60 to 90% reduction of *rankl* expression by each primer set in all animals tested (Fig. 3.8c), suggesting that the function of *rankl* is largely repressed in *rankl* gRNA-injected adult animals. However, the size and morphology of scales were nearly unaffected in *rankl* gRNA-injected animals (Fig. 3.8d). In mice, *Rankl* deficiency leads to reduction in the number of multinucleated OCs in the bone tissue (Kong et al., 1999). Consistent with *Rankl*-deficient mice, *rankl* gRNA-injected zebrafish decreased in both the percentage and number of *trap:GFP*[high] OCs compared with uninjected control zebrafish. By contrast, the number of OBs (GFP[−] mCh[+] Hoe[high] fraction) and OB-derived EVs (mCh[+] Hoe[low] fraction) was unchanged in *rankl*-gRNA-

injected zebrafish (Fig. 3.9), suggesting that loss of *rankl* does not affect production and secretion of EVs in OBs. KMCs from wild type *trap:GFP* animals were co-cultured with OBs (mCh$^+$ Hoe^{high}) or EVs (mCh$^+$ Hoe^{low}) from wild type or *rankl* gRNA-injected *osterix:mCherry* animals. The number of *trap:GFP$^+$* cells significantly decreased in cells co-cultured with EVs from *rankl* gRNA-injected animals compared with those from wild type animals, while there were no significant differences between cells co-cultured with OBs from wild type and *rankl* gRNA-injected animals (Fig. 3.8e). Collectively, these data suggest that OC differentiation is promoted by uptake of OB-derived EVs in a Rankl dependent manner.

4. Discussion

In this chapter, transplantation assays and imaging analysis suggest that immature OCs engulf OB-derived EVs before convergence at the fracture site. In addition, cell culture assays revealed that OB-derived EVs promote the differentiation of OCs from hematopoietic cells via Rankl signaling. These findings provide novel insights into the regulatory mechanisms underlying OC differentiation by OBs in the bone tissue.

Both metabolic and genetic bone diseases are associated with the disruption of the intercellular communication between OCs and OBs. The regulatory mechanisms of osteoclastogenesis by OBs have been elucidated by many in vitro studies using murine cell lines. The precursor of monocytes/macrophages can give rise to OCs in the presence of M-CSF and RANKL. M-CSF is a secreted cytokine that is expressed in part by OBs and binds to c-Fms expressed on OCs to regulate the migration, survival, and bone resorption activity (Cappariello et al., 2014). RANKL-RANK signaling activates the TNF receptor-associated factor (TRAF) family, which regulates the formation, survival, and

activation of OCs through multiple signaling pathways (Cappariello et al., 2014; Chen et al., 2018). Thus, in vitro studies have elucidated molecular functions that are involved in OC differentiation. It is still challenging, however, to investigate the interaction of OBs and OCs in vivo, and hence cell-cell communication between these two types of cells remain largely unknown. Ishii's group utilized intravital two-photon imaging to visualize the behavior of living OCs in mouse bone. They found two subsets of functional OCs based on their motility and function, 'static – bone resorptive' and 'moving – non resorptive', which can be converted by a direct contact with OBs (Kikuta et al., 2013). There are also two types of OCs in the amputated medaka fin, early-induced and late-induced OCs. The former is relatively small cells that show low TRAP-activity and resorb bone fragments, while the latter is large cells that show high TRAP activity and remodel the callus (Takeyama et al., 2014). These analyses provided insight into the functional divergence of OCs, indicating the importance of live-imaging analysis in vivo to understand the function of OCs and OBs. The model system using the transgenic zebrafish scale established here enables to visualize the whole tissue at the single cell level throughout the process of fracture healing. Indeed, the moment of cell-cell fusion between two OCs, the convergence of OCs at the fracture site, and uptake of OB-derived EVs by OC precursors has been successfully captured in the fractured scale. The imaging strategy in the zebrafish scale may open new avenues to elucidate molecular cues needed to regulate cell-cell communication in the bone tissue.

The double-transgenic zebrafish, *trap:GFP*; *osterix:mCherry*, is also useful to examine the role of EVs in the bone tissue. EVs have been recognized as potent vehicles of intercellular communication. EVs released by a variety of cells transport biologically active molecules, such as proteins, lipids, mRNAs, and microRNAs to target cells;

however, our current knowledge regarding the roles of EVs is still very limited (Tkachi et al., 2016). It is reported that a transgenic zebrafish line that expresses human CD63 fused with pHluorin under the control of the specific enhancer can be used to visualize EVs in vivo (Noishiki et al., 2019). It is also reported in zebrafish that tracking of EVs released from melanoma cells in embryos determined the role of EVs in the formation of metastatic niches, highlighting that zebrafish is an elegant model for the study of EVs. In this chapter, transplantation assays clearly demonstrated that mCherry$^+$ particles observed in the cytoplasm of *trap:GFP$^+$* cells are derived from EVs released by OBs. FCM analysis revealed that approximately 75% of *trap:GFP*^{high} cells contains mCherry$^+$ EVs at 1 d.p.fr., suggesting that the majority of OCs engulf OB-derived EVs during the process of differentiation. These data strongly suggest that cell communication between OCs and OBs largely depends on the release and uptake of EVs. In addition, cell culture assays revealed that OB-derived ABs also promote OC differentiation, raising the possibility that apoptosis of OBs induces the differentiation of OCs to initiate bone resorption. Because OCs arise from the precursor of monocytes/macrophages, phagocytosis of OB-derived ABs also triggers OC differentiation. Such EV-mediated cell-cell communication between OCs and OBs represents a novel regulatory mechanism in the bone tissue. Further studies of EVs in bone tissue will uncover the molecular mechanisms underlying bone resorption and formation.
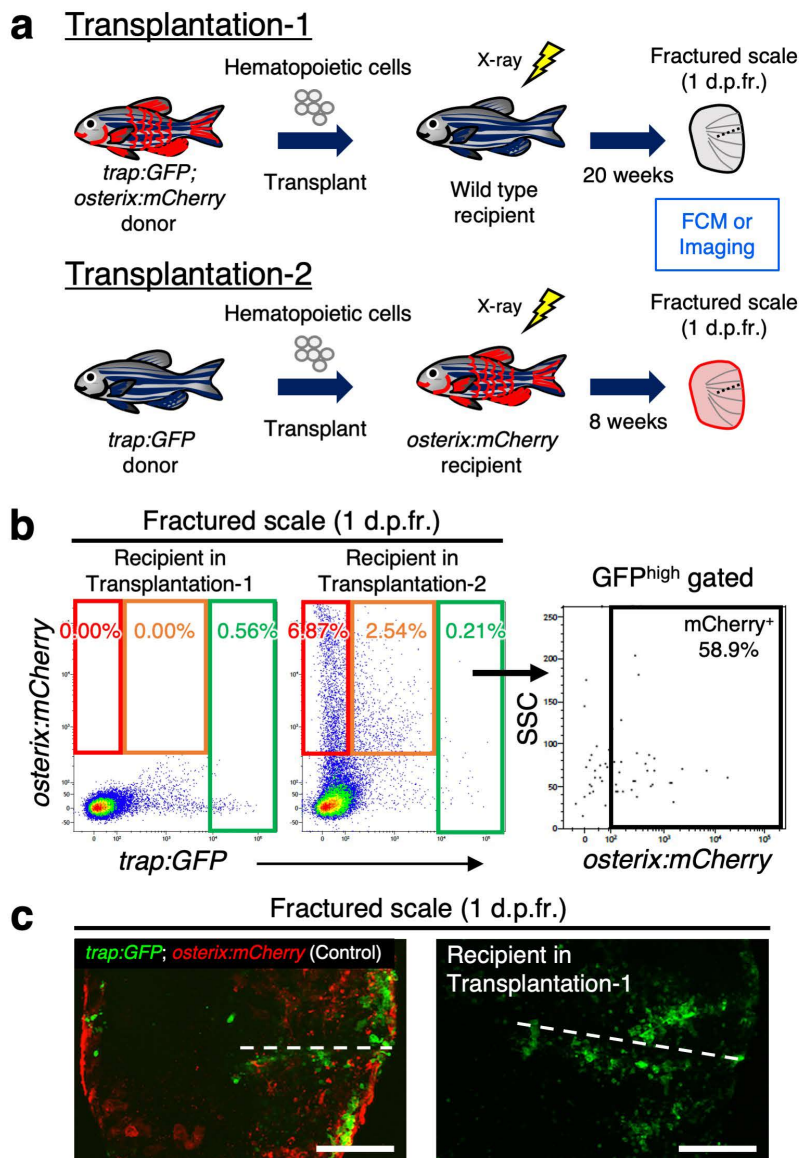
Figure 3.1 Transplantation assays confirm uptake of OB-derived EVs in OCs.

(**a**) Schematic diagram of transplantation assays. Hematopoietic cells from the kidney of *trap:GFP*; *osterix:mCherry* double-transgenic zebrafish were transplanted into wild type recipients irradiated with sublethal dose of X-ray (Transplantation-1). Hematopoietic cells from *trap:GFP* single-transgenic zebrafish were transplanted into *osterix:mCherry* single-transgenic recipients (Transplantation-2). At 20 or 8 weeks post-transplantation, cells in scales at 1 d.p.fr. were examined by FCM and/or confocal microscopy. (**b**) Representative FCM results in fractured scales from a recipient in Transplantation-1 (left) and Transplantation-2 (midle). Red, orange, and green gate show mCh+, GFPlow, and GFPhigh cells, respectively. GFPhigh cells in a recipient of Transplantation-2 are displayed in an *osterix:mCherry* vs. side scatter (SSC) plot (right panel). (**c**) Fluorescent images of a fractured scale from a *trap:GFP*; *osterix:mCherry* double-transgenic animal (left) and recipient in Transplantation-1 (right). Dotted lines indicate the fracture site. Bars, 100 μm.
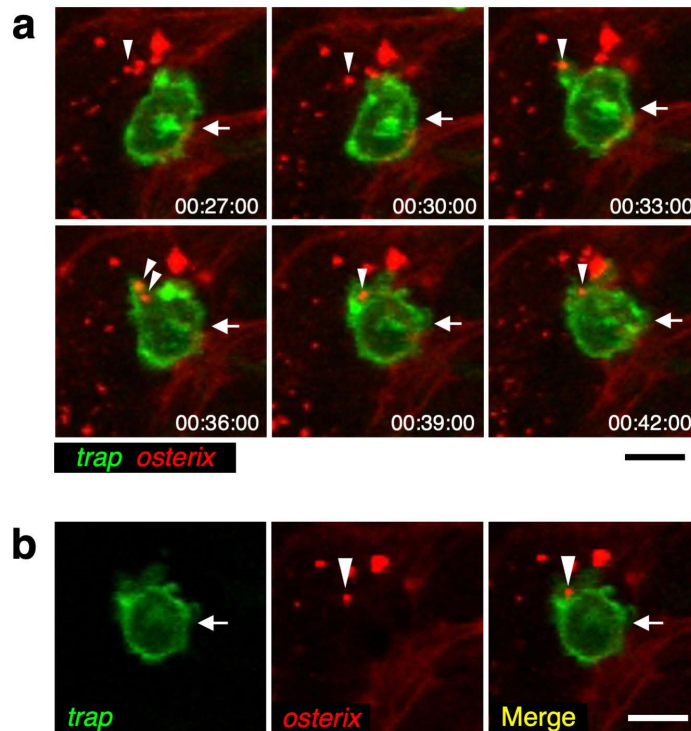
Fig 3.2 Time-lapse imaging of a fractured scale in a *trap:GFP*; *osterix:mCherry* double-transgenic zebrafish.

(**a**) Six sequential snapshots are shown. Arrows and arrowheads indicate a *trap:GFP*[+] OC and mCherry[+] particle, respectively. The *trap:GFP*[+] OC extended a protrusion and engulfed mCherry[+] particles. (**b**) Single plane of a z-stack of a *trap:GFP*[+] cell at 39 min. Images show a green (*trap:GFP*), red (*osterix:mCherry*), and merged channel. Bars, 10 µm.

a Fractured scale (1 d.p.fr.)

mCh⁺ Hoe^high

mCh⁺ Hoe^low (EVs)

Hoechst 33342

mCh⁺ Hoe^high

mCh⁺ Hoe^low

osterix:mCherry

SSC

FSC

b mCh⁺ Hoe^low (EVs)

c Diameter of EVs (μm)

% Distribution

-0.6 0.6 - 0.8 0.8 - 1.0 1.0 - 1.5 1.5 - 2.0 > 2

d

**

\# EVs / scale

Intact Fractured
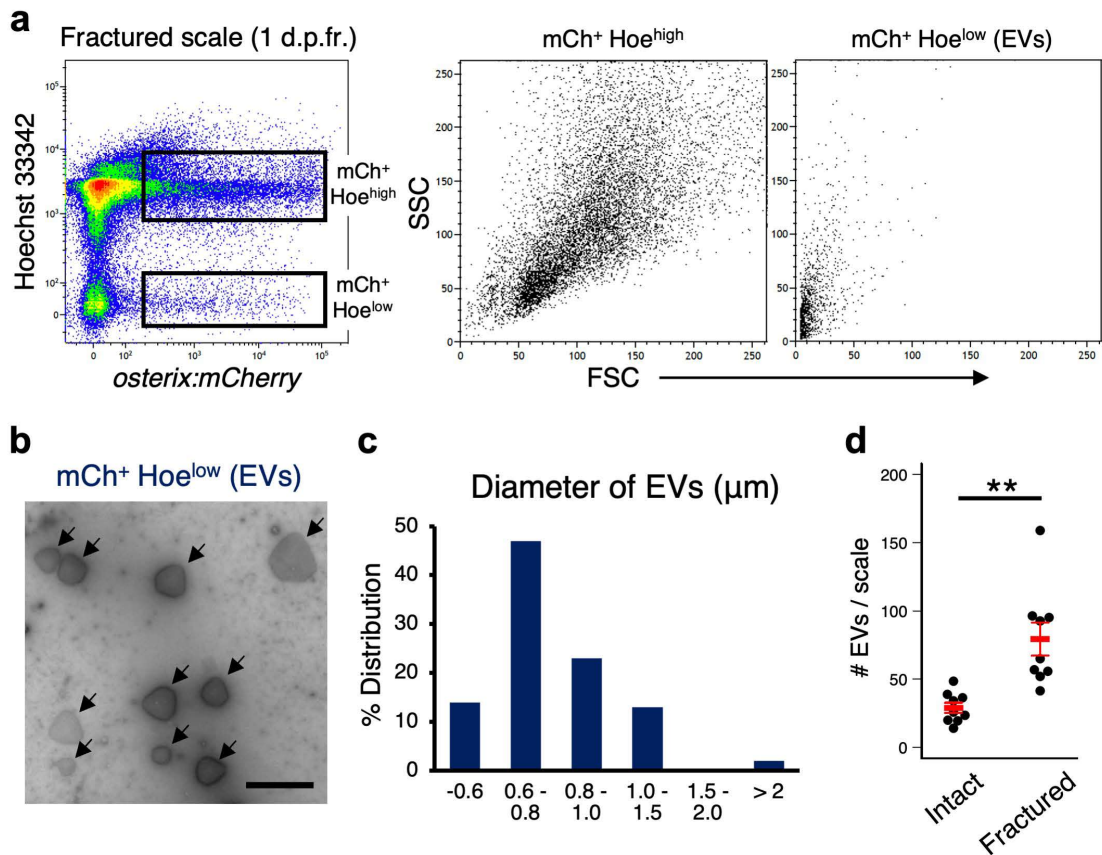
Figure 3.3 Isolation of OB-derived EVs.

(**a**) Representative FCM results of cells in fractured scales at 1 d.p.fr. from an *osterix:mCherry* single-transgenic zebrafish. Gated regions in the left panel indicate the fraction of *osterix:mCherry*⁺ Hoecht 33342^high (mCh⁺ Hoe^high) and mCh⁺ Hoe^low EV. mCh⁺ Hoe^high cells and mCh⁺ Hoe^low EVs are displayed in a forward scatter (FSC) vs. side scatter (SSC) plot (middle and right panels, respectively). (**b**) Negative staining of isolated EVs. Arrows in indicate an EV. Bars, 1 μm. (**c**) Percent size distribution of EVs. (**e**) Absolute number of mCh⁺ Hoe^low EVs in an intact and fractured scale at 1 d.p.fr.. ****p < 0.01.
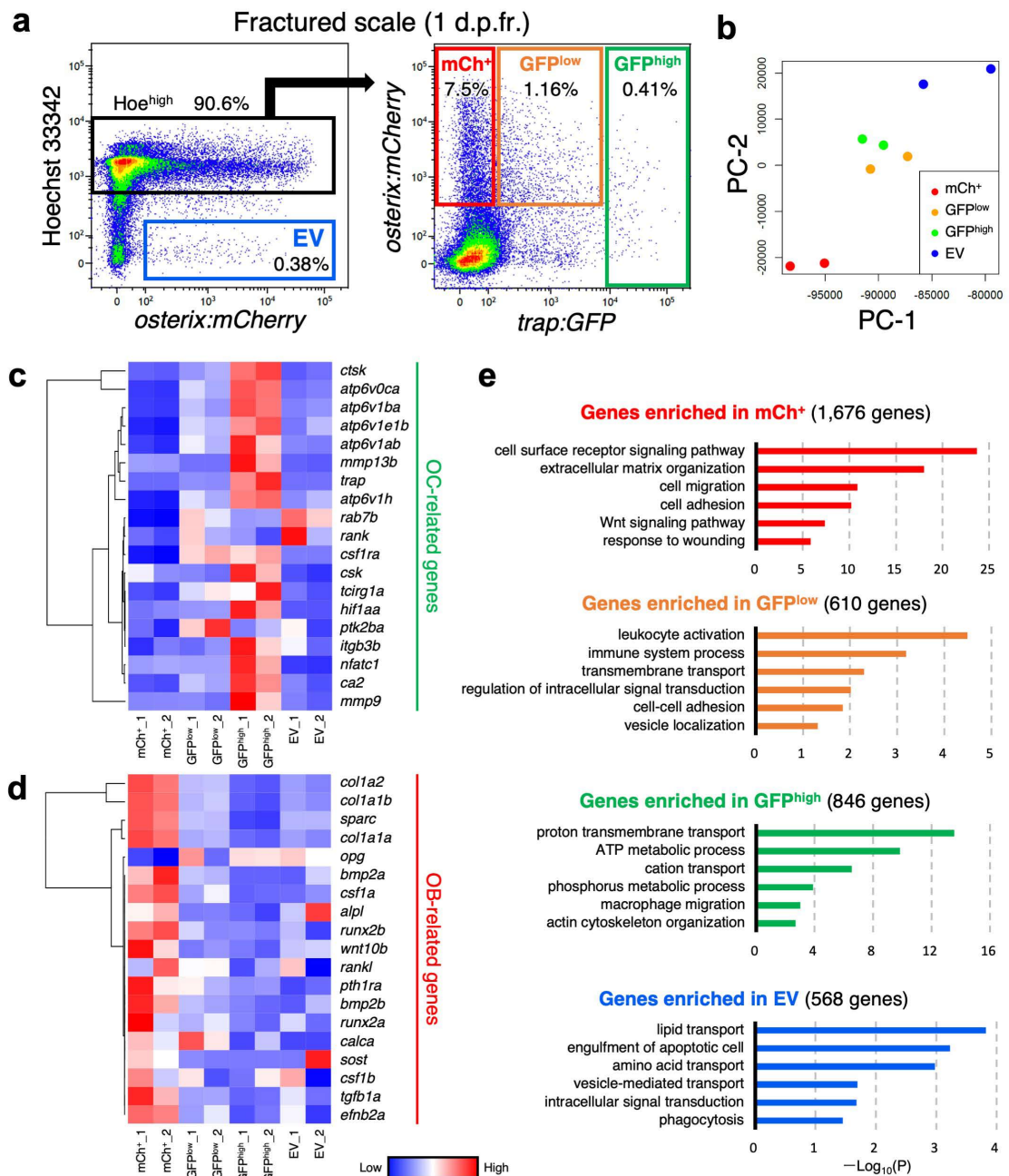
Figure 3.4 Transcriptome analysis of OBs, OCs, and OB-derived EVs.

(**a**) Representative FCM results of cells in scales at 1 d.p.fr. from a *trap:GFP*; *osterix:mCherry* double-transgenic zebrafish. Gated regions in the left panel indicate the fraction of Hoechst 33342[high] (Hoe[high]) and *osterix:mCherry*[+] Hoe[low] ("EV"). Cells in the Hoe[high] fraction are displayed in the right panel to further divide into three populations, mCh[+], GFP[low], and GFP[high]. (**b**) Principal component analysis (PCA) based on the tags per million (TPM) of each sample. (**c**, **d**) Hierarchical clustering of selected OC-related (**c**) and OB-related genes (**d**) in the mCh[+], GFP[low], GFP[high], and EV fraction. (**e**) Gene ontology enrichment analysis of differentially expressed genes in the mCh[+], GFP[low], GFP[high], and EV fraction.
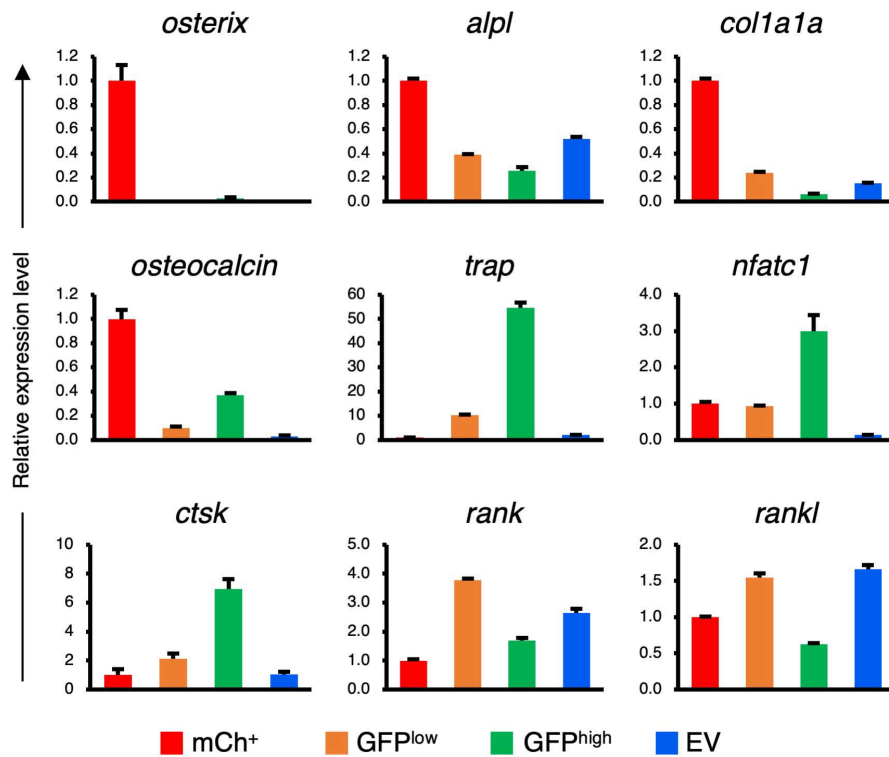
Figure 3.5 Gene expression analysis of OBs, OCs, and OB-derived EVs.

The expression of *osterix*, *alpl*, *col1a1a*, *osteocalcin*, *trap*, *nfatc1*, *ctsk*, *rank*, and *rankl* in the mCh+, GFPlow, GFPhigh, and EV fraction at 1 d.p.fr. Error bars, s.d.

a Fractured scale (1 d.p.fr.)

mCh$^+$ Hoe^{high} 6.77%

mCh$^+$ Hoe^{low} 0.74%

Hoechst 33342

osterix:mCherry

b

mCh$^+$ Hoe^{high} cells

Apoptotic cells 10.93%

Live cells 79.19%

Pre-apoptotic cells 7.47%

Sytox Red

mCh$^+$ Hoe^{low} EVs

MVs 64.56%

ABs 34.29%

Annexin V-FITC

c Hematopoietic cells

Co-culture for 2 days

trap:GFP

osterix:mCherry Fractured scale (1 d.p.fr.)

OBs or MVs or ABs

d

GFP$^+$ cells

** *** **

Control + OBs + MVs + ABs

e + OBs   + MVs   + ABs

trap *osterix* DAPI

Figure 3.6 OB-derived EVs facilitate OC differentiation.

(**a**) Representative FCM results of cells in scales at 1 d.p.fr. from a *osterix:mCherry* single-transgenic zebrafish. Gated regions indicate the mCh$^+$ Hoe^{high} cell fraction and mCh$^+$ Hoe^{low} EV fraction. (**b**) mCh$^+$ Hoe^{high} cells and mCh$^+$ Hoe^{low} EVs were shown in an Annexin-V-FITC vs. Sytox Red plot. mCh$^+$ Hoe^{high} cells were subdivided into three fractions, "live", "pre-apoptotic", and "apoptotic", while mCh$^+$ Hoe^{low} EVs were divided into two fractions, "microvesicle" (MV) and "apoptotic body" (AB). (**c**) Schematic diagram of in vitro cell culture assays. Hematopoietic cells from the kidney of *trap:GFP* single-transgenic zebrafish were co-cultured with OBs, MVs, or ABs from fractured scales of *osterix:mCherry* single-transgenic zebrafish on a fibronectin-coated plate. At 2 days of co-culture, the number of *trap:GFP$^+$* cells was counted in each well. Non-co-cultured hematopoietic cells were used as a control. (**d**) The average number of *trap:GFP$^+$* cells in each well. Error bars, s.d., (**e**) Images of *trap:GF*P$^+$ cells co-cultured with OBs (left panel), MVs (middle panel), or ABs (right panel). *trap:GFP$^+$* cells contained OB-derived EVs in the cytoplasm (arrows). Bars, 5 μm.
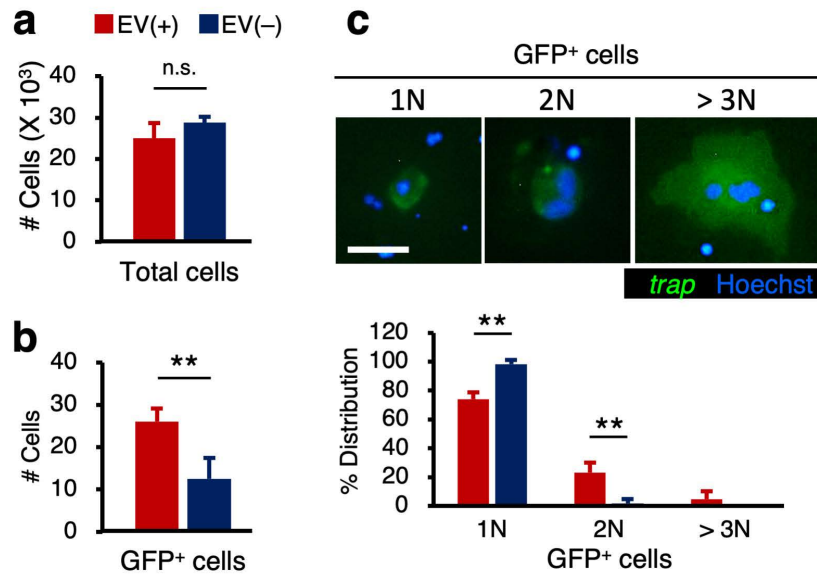
Figure 3.7 Treatment of EVs promotes differentiation and fusion of OCs.

(**a**, **b**) The number of total cells (**a**) and GFP+ cells (**b**) in the presence or absence of OB-derived EVs. Error bars, s.d., (**c**) Images of *trap:GF*P+ cells co-cultured with EVs (upper panel) and percent distribution of GFP+ cells possessing a single nucleus (1N) or two (2N) or more than three nuclei (3N) in the presence and absence of EVs. Bar, 20 µm; **p < 0.01.
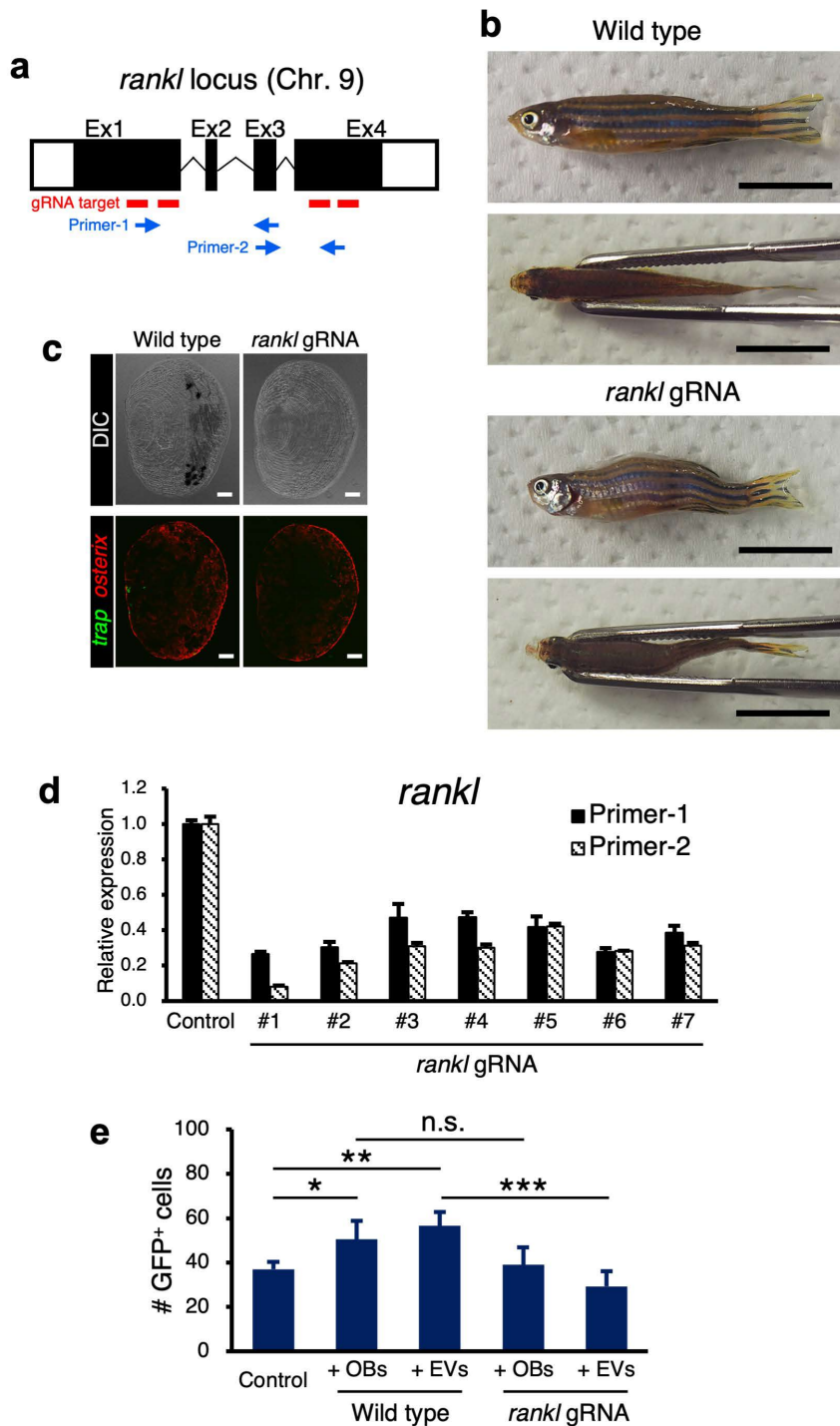
Figure 3.8 Loss of *rankl* in OB-derived EVs impaires the promotion of OC differentiation.

(**a**) Schematic diagram of the zebrafish *rankl* locus. Red bars and blue arrows indicate a gRNA target site and primer recognition site, respectively. (**b**, **c**) Representative images of a wild type or *rankl* gRNA-injected zebrafish and their scale at 4 months of age. *rankl* gRNA-injected zebrafish showed severe body curvature, although scales were normally formed. Bars, 1 cm (**b**); 200 μm (**c**). (**d**) Relative expression level of *rankl* mRNAs in the fin of an individual *rankl* gRNA-injected or uninjected control zebrafish. (**e**) The number of *trap:GFP*+ cells in cultured hematopoietic cells of each group.

a

Wild type / *rankl* gRNA

osterix:mCherry

Wild type:
mCh+ 5.47% GFPlow 3.31% GFPhigh 0.58%

rankl gRNA:
mCh+ 6.42% GFPlow 2.73% GFPhigh 0.04%

trap:GFP

b

GFPhigh — % cells — **

Total — # cells / scale (X 10^3) — n.s.

mCh+ — # cells / scale — n.s.

GFPlow — # cells / scale — n.s.

GFPhigh — # cells / scale — **

mCh+ Hoelow (EV) — # EVs / scale — n.s.

Wild type / *rankl* gRNA
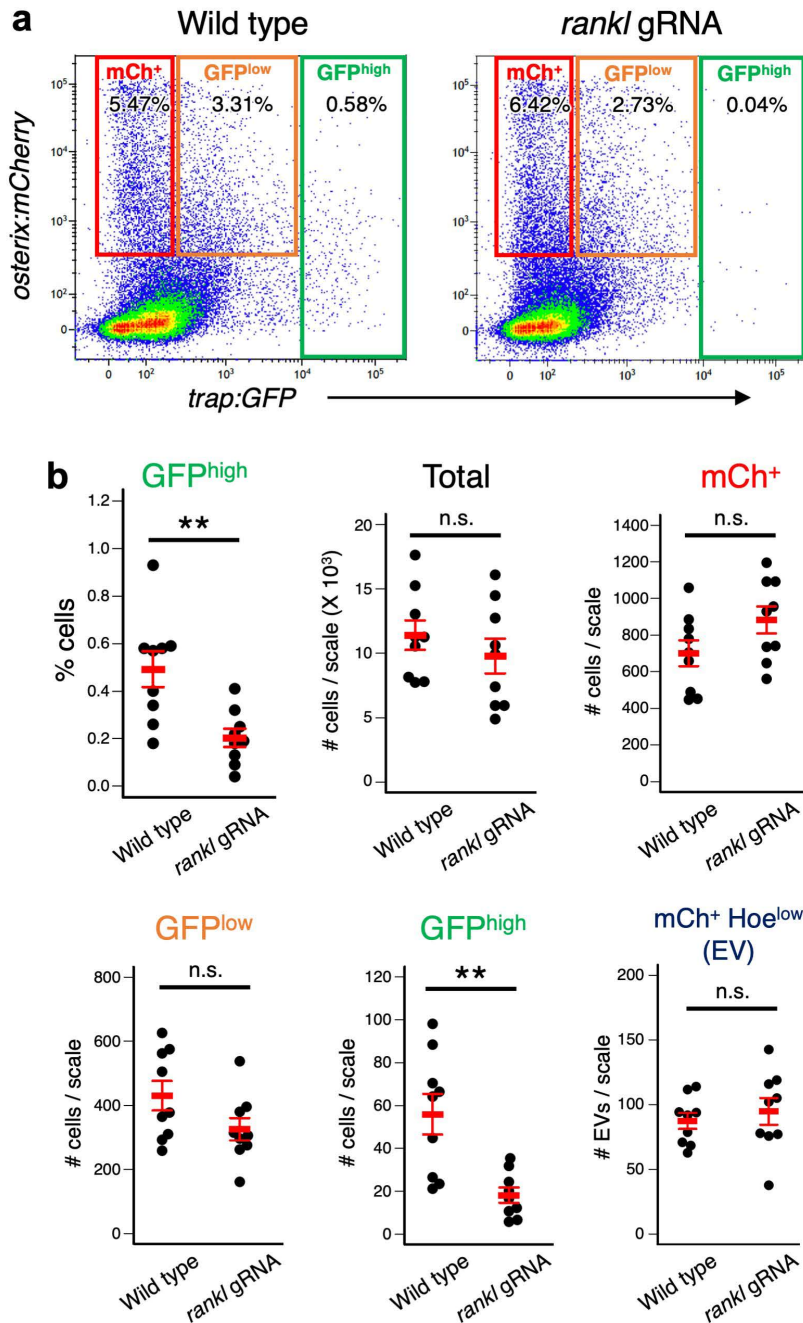
Figure 3.9 GFPhigh OCs significantly decrease in the fractured scale of *rankl* gRNA- injected zebrafish

 (**a**) Representative FCM results of cells in fractured scales at 1 d.p.fr. from a wild type or *rankl* gRNA-injected zebrafish. Red, orange, and green gate show mCh+, GFPlow, and GFPhigh cells, respectively (**b**) Percentage or absolute number of GFPhigh, total, mCh+, GFPlow cells, and mCh+ Hoelow EVs in a fracture scale of wild type or *rankl* gRNA-injected zebrafish at 1 d.p.fr. Error bars, s.e.m (n = 9 for each group); n.s., no significance; **$p <$ 0.01.

Table 2 Primers in the thesis

Gene	Forward primer	Reverse primer	Description
trap (zebrafish enhancer)	CTCGAGGAGATGTAACTTCCAACACTC	GGATCCCCCTACAAAACAACATACAAACAG	Generation of transgenic line
osterix (medaka enhancer)	CTCGAGTGAACATGTCAGTGCCATCAG	GGATCCCGGGACAGTTTGGAAGAAGTC	Generation of transgenic line
ef1a	ACCGGCCATCTGATCTACAA	CAATGGTGATACCACGCTCA	qPCR
osterix	ATTGACCCTCACTGGACTGC	ACCAGGTGTGGCAGAATCTC	qPCR
alpl	GAGAAGCGGCCTGATTACTG	GTCTTAGAGAGGGCGACGTG	qPCR
col1a1a	TTTTGGCAAGAGGACAAGGC	TGTCTTCGCAGATCACTTCG	qPCR
osteocalcin	CTGCTGCCTGATGACTGTGT	TCCAGACGTGTCCATCATGT	qPCR
trap1	ATGATGGCCAAAACTGCTTC	CAGCAATGACGTACCAAGGA	qPCR
nfact1	TCACTGCCTGCTCTTGATTG	CCTGGTAGAATGCGTGAGGT	qPCR
ctsk	GAGGGAGTACAATGGCCTGA	CCGAAGTGACGTATCCCAGT	qPCR
rank	AATCGCACGGTTATTGTTGTT	ACTGCAGCAA AGTCCCAGTT	qPCR
rankl	TAGTGTGGCGATTCTGTTGC	ATTGGAAGGTGAGCTGATGG	qPCR (primer-1)
rankl	CCATCAGCTCACCTTCCAAT	CGAAA ACAGGTCTTGGCGTA	qPCR (primer-2)
mtnr1ab	CCACAACTTTGGGCAGTTTT	ATCTGGCAGTGGACAAATCC	qPCR
mtnr1c	GCTGGTCATCTTGTCCGTCT	CTGAGCCGATCACACTCAGA	qPCR
epcam	CGATGAAGTGGGCAAACTG	AGGCAGTCTCAACTGGCTTC	qPCR
il6	GTCCCCGTGTTCAGCAGTAT	CTGATCCTGACCCCTTCAAA	qPCR
tnfa	TCTGCTTCACGCTCCATAAG	TAAATGCCATCATCGGGAAT	qPCR

Table 3 Oligoes in the thesis

Primers sequence for whole-transcript amplification	Description
TATAGAATTCGCGGCCGCTCGCGATAATACGACTCACTATAGG GCGTTTTTTTTTTTTTTTTTTTTTTTTT	RT primer
TATAGAATTCGCGGCCGCTCGCGATTTTTTTTTTTTTTTTTTTTTTT TTT	Tagging primer
(5' Aminolink)-GTATAGAATTCGCGGCCGCTCGCGAT	Suppression primer

CRISPR/Cas9	Description
TAATACGACTCACTATAGGTGCAGGTCGCGTCTAGTGGTTTTA GAGCTAGAAAT AGC	*rankl* target-1
TAATACGACTCACTATAGGTAACCGGTTATCTCCGAGGTTTTAG AGCTAGAAATAGC	*rankl* target-2
TAATACGACTCACTATAGGTATACATAGTAGTATCCAGTTTTAG AGCTAGAAATAGC	*rankl* target-3
TAATACGACTCACTATAGGTCTCATGGTATCGAAAACGTTTTAG AGCTAGAAATAGC	*rankl* target-4
AAAAGCACCGACTCGGTGCCACTTTTTCAAGTTGATAACGGAC TAGCCTTATTTTAACTTGCTATTTCTAGCTCTAAAAC	gRNA scaffold primer

Chapter 4

Melatonin suppresses OB and OC differentiation

through epidermal ERK signaling

1. Introduction

The most common chronic metabolic bone disease, osteoporosis, has become a public health concern worldwide, carrying huge economic burden every year (Tu et al., 2018, Noh et al., 2020). Since osteoporosis occurs as a result of the unbalance between bone resorption and formation, either antiresorptive (e.g. bisphosphonates, estrogen agonist/antagonists, estrogens, calcitonin and denosumab) or anabolic agents (e.g. teriparatide) are used to deal with osteoporosis. Antiresorptive medications primarily work on decreasing the rate of bone resorption by suppressing OC activity, while anabolic treatment increases bone formation relatively than bone resorption.

An analog of recombinant human parathyroid hormone (PTH), teriparatide, is the first anabolic treatment approved for osteoporosis (Tu et al., 2018). It shows the effect to decrease the risk of fracture in osteoporotic patients and potentially enhance bone mineral density (Neer et al., 2001; Black et al., 2003). Campbell et al. examined the effect of PTH combined with alendronate, a bisphosphonate medication used to treat osteoporosis, on the bone architecture, mineralization, and estimated mechanics in ovariectomized rats and found that substantial improvement in every aspect compared to monotherapy (Campbell et al., 2011). Once-daily injection of teriparatide initially increases biochemical markers of bone formation and resorption, then peaks at 6-12 months, but declines in bone formation despite continued treatment (Wu et al., 2011). Suzuki et al. developed a new in vitro assay system using the goldfish scale to investigate the effect of fugu PTH1 on OBs and OCs. Fugu PTH1 significantly enhanced ALP activity in OBs and TRAP activity in OCs (Suzuki et al., 2011). It is reported, however, that prolonged treatment with hPTH in rats results in development of bone tumors, providing evidence that the usage of hPTH should be limited to 2 years (Vahle et al., 2002; Tu et al., 2018). Thus, additional drug

candidates that repress bone resorption during bone formation are needed to treat osteoporosis.

Melatonin is the major pineal hormone that is involved in circadian rhythm regulation and also bone metabolism (Einhorn et al., 2015; Histing et al., 2012; Ladizesky et al., 2003; Jiang et al., 2019; Liu et al., 2016; Ostrowska et al., 2002; Park et al., 2011; Satomura et al., 2007). In vitro studies in mammals revealed that melatonin treatment promotes the proliferation of OBs and enhances the expression of OB-related proteins, including osteopontin, alkaline phosphatase (ALP), osteocalcin, and bone sialoprotein, to stimulate the formation of mineralized bone matrix (Li et al., 2019). In addition, melatonin inhibits OC differentiation via the downregulation of RANK and the upregulation of osteoprotegerin (OPG), encoding an inhibitor of RANK (Kim et al., 2017). These suggest that melatonin promotes bone formation, but represses bone resorption. A few in vivo studies, however, demonstrated the inhibitory effect of melatonin on fracture healing. Injection of melatonin in a femur fracture-model mouse impairs fracture healing through repression of RANKL-mediated OC activation (Einhorn and Gerstenfeld, 2015). In rats, the daily secretion of melatonin is negatively correlated with the profile of biochemical markers of bone formation (Laduzesjy et al., 2003). Thus, the effect of melatonin on OCs and OBs is still controversial and the role of melatonin in bone metabolism remains to be elusive.

In this chapter, the effect of melatonin treatment on OBs and OCs was investigated in vivo using the double transgenic line, *trap:GFP*; *osterix:mCherry*. Treatment with melatonin resulted in the repression of extracellular signal-regulated kinase (Erk) signaling, a component of the mitogen-activated protein kinase (MAPK) cascade, in epidermal cells of the scale, leading to reduction in the number of OBs and OCs at the

fracture site during the early stage of fracture healing.

2.   Materials and Methods

2.1 Zebrafish maintenance

Zebrafish were kept as described in Chapter 2 (Materials and Methods 2.1). For chemical treatment, zebrafish were treated in system water containing dimethyl sulfoxide (DMSO), melatonin (40μM in DMSO), or SL-327 (1μM) for 1 day upon induction of fracture.

2.2 Immunohistochemistry

Intact and fractured scales were removed and fixed with 4% PFA in PBS overnight and washed with gradient methanol in 0.1% Tween-20 (Sigma) in PBS (PBT). After rehydration with PBT, scales were blocked with 2% blocking regent (Roche) in PBT, followed by staining with primary antibodies, rabbit anti-RFP antibody (for staining mCherry; 1:1000) (Abcam), chicken anti-GFP antibody (1:1000) (Aves), and rabbit anti-phosphorylated Erk1/2 antibody (1:250) (Cell Signaling Technology), at 4℃ overnight. Scales were washed with PBT and stained with secondary antibodies, goat anti-chicken IgY-Alexa 488 and goat anti-rabbit IgG-Alexa 647 (1:1000) (Abcam), at 4℃ overnight. Scales were then washed with PBT and mounted in 0.6% low-gelling agarose for imaging.

2.3 Flow cytometry

Cells in the scale were collected from DMSO, melatonin, or SL-327-treated zebrafish as described in Chapter 2 (Materials and Methods 2.3). Acquisition, cell sorting, and cell counting were performed as described in Chapter 2 (Materials and Methods 2.3).

2.4 Intubation anesthesia and confocal imaging

Intubation anesthesia was performed as described in Chapter 2 (Materials and Methods 2.4). Fluorescent images were captured using an FV10i confocal microscope and Fluoview FV10i-SW software (ver. 2.1.1) (Olympus) as described in Chapter 2 (Materials and Methods 2.4). The convergence area of *trap:GFP*^{+} cells in each scale was measured according to the intensity value of GFP obtained from the FV10-ASW4.2 software (Olympus).

2.5 Quantitative PCR

RNA extraction, cDNA preparation, and quantitative polymerase chain reaction (qPCR) were performed as previously described in Chapter 3 (Materials and Methods 2.6). Primers used for qPCR are listed in Table 2.

2.6 Statistical analysis

Statistical significance between groups was determined as described in Chapter 2 (Materials and Methods 2.6).

3. Results

3.1 Melatonin treatment suppresses OC convergence at the fractured site

To examine the effect of melatonin on fracture healing in the zebrafish scale, the epidermis area of the scales in double-transgenic zebrafish (*trap:GFP*; *osterix:mCherry*) was cut, and these animals were treated with DMSO (vehicle) or melatonin. The dynamics of *trap:GFP*[+] OCs and *osterix:mCherry*[+] OBs was monitored by confocal microscopy. As shown in chapter 3, *trap:GFP*[+] OCs are detected at the edge of the scale

near the fracture site where *osterix:mCherry*[bright] OBs are frequently observed at 1 d.p.fr. These *trap:GFP*[+] OCs actively interact with *osterix:mCherry*[bright] OBs and fuse to form a multinucleated mature OC before converging at the fracture site. Consistent with this observation, *trap:GFP*[+] OCs in DMSO-treated zebrafish were observed along the edge of the scale at 1 d.p.fr., and near the fracture site by 2 d.p.fr. In contrast, only a few *trap:GFP*[+] OCs were observed in melatonin-treated zebrafish, leading to the fewer number of OCs at the fracture site at 2 d.p.fr. (Fig. 4.1a). Compared with DMSO-treated zebrafish, both the coverage area of *trap:GFP*[+] OCs and mean fluorescent intensity of GFP expression in the fracture site significantly decreased in melatonin-treated zebrafish at 1 and 2 d.p.fr. (Fig. 4.1b). These data suggest that differentiation of OCs under fracture stress is suppressed by melatonin treatment.

3.2 Melatonin treatment decreases the number of OBs and OCs

To further examine the effect of melatonin on fracture healing, the number of OBs and OCs was quantified in the scale at 1 d.p.fr. by flow cytometry. As shown in chapter 3, mature OCs with one to three nuclei can be found in the *trap:GFP*[high] fraction at 1 d.p.fr., whereas monocytes/macrophages, including precursors of OCs, were observed in the *trap:GFP*[low] fraction. Due to the uptake of OB-derived EVs, most *trap:GFP*^{+} cells are detected in the *osterix:mCherry*[+] fraction. Both *trap:GFP*[+] OCs and *osterix:mCherry*[+] OBs were detected in the scale of DMSO- or melatonin-treated zebrafish at 1 d.p.fr. (Fig. 4.2a). However, both the percentage and absolute number of OC fractions, *trap:GFP*[low] *osterix:mCherry*[+] ("GFP[low]") and *trap:GFP*[high] ("GFP[high]"), significantly decreased in melatonin-treated zebrafish compared with DMSO-treated zebrafish (Fig. 4.2b), confirming that OC differentiation is suppressed by melatonin treatment. In addition, a

fewer number of *trap:GFP⁻ osterix:mCherry⁺* ("mCh⁺") OBs were also observed in melatonin-treated zebrafish (Fig. 4.2b). These results suggest that treatment with melatonin impairs the differentiation of both OBs and OCs in the fractured scale.

Opposite results were obtained in PTH-treated zebrafish. Treatment of PTH led to the increased percentage of GFP^{high} OCs and mCh⁺ OBs at 1 d.p.fr. (Fig 2.6b), suggesting that PTH treatment promotes the differentiation of both OBs and OCs in the fractured scale.

3.3 Melatonin receptors are predominantly expressed by epithelial cells in the scale

To investigate which cell types express melatonin receptors in the zebrafish scale, qPCR analysis was performed in four different cell fractions of the fractured scale, mCh⁺ (OBs), GFP^{low} (monocytes/macropages), GFP^{high} (OCs), and double-negative (DN) cells (Fig. 4.3a). Unexpectedly, the expression level of melatonin receptor genes, *mtnr1ab* and *1c*, was higher in the DN fraction compared with other fractions (Fig. 4.3b), while other receptor genes (*mtnr1aa*, *1ba*, and *1bb*) were undetectable in all four cell fractions (data not shown). Cells in the DN fraction expressed an epithelial marker gene, *epcam* (epithelial cell adhesion molecule), but not an OB marker gene, *alpl*, or OC marker genes, *trap* and *ctsk* (Fig. 4.3c). These results suggest that melatonin receptors were mainly expressed by epithelial cells in the zebrafish scale.

3.4 Melatonin represses Erk signaling in epidermal cells of the fractured scale

It is known that melatonin inhibits the proliferation of osteosarcoma cells through suppression of Erk signaling (Liu et al., 2016), leading to promotion of osteogenic differentiation (Ladizesky et al., 2003; Park et al., 2011; Kobayashi et al., 2020). These

observations allow us to investigate the level of Erk signaling in the fractured scale. Immunohistochemistry analysis using an antibody against phosphorylated Erk1 and 2 (pErk1/2), the activated form of Erk1/2, showed that pErk1/2 signals largely increased in *osterix:mCherry*-negative epidermal cells in response to fracture stress (Fig. 4.4a,b). In contrast, pErk1/2 signals did not increase in the fractured scale of melatonin-treated zebrafish (Fig. 4.4a), in which fewer *trap:GFP*+ OCs were detected. These results suggest that epidermal Erk signaling is enhanced by fracture stress, but this enhancement is inhibited by melatonin treatment. To establish the link between fracture healing and Erk signaling, scale-fractured zebrafish were treated with a MEK inhibitor, SL-327, to decrease Erk signaling. Similar with melatonin-treated animals, SL-327-treated zebrafish showed a reduced number of *trap:GFP*+ OCs at the edge region near the fracture site at 1 d.p.fr. (Fig. 4.4a). Furthermore, the number of both mCh+ OBs and GFP^{high} OCs significantly decreased in SL-327-treated zebrafish compared with DMSO-treated zebrafish (Fig. 4.4c, d). These results suggest that epidermal Erk signaling promotes the differentiation of both OBs and OCs in the fractured scale.

Inflammatory cytokines secreted by immune cells in bone tissue induces the differentiation of both OBs and OCs in mammals (Baht et al., 2018; Einhorn and Gerstenfeld, 2015), suggesting that secretion of inflammatory cytokines by immune cells may be one of the earliest signals to induce OB and OC differentiation. Because melatonin treatment blocks early OB and OC differentiation in the zebrafish scale, the next study is intended to investigate if treatment with melatonin or SL-327 changes the expression of inflammatory cytokine genes in the fractured scale. The expression of *il6* (*interleukin 6*) and *tnfa* (*tumor necrosis factor a*) was largely upregulated in the fractured scale at 1 d.p.fr. compared with the intact scale. Upregulated expression was also observed in the fractured

scale of melatonin- or SL-327-treated zebrafish (Fig. 4.4e). Collectively, these results suggest that melatonin inhibits OC and OB differentiation independently of inflammatory cytokine signals in the zebrafish scale.

4. Discussion

In vivo studies in this chapter demonstrated that melatonin induces a marked suppression of both OB and OC differentiation in the zebrafish scale, as evidenced by significantly reduced numbers of OCs and OBs during the early period of fracture healing. Treatment with melatonin leads to reduced epidermal pErk1/2 signals in the fractured scale without affecting the expression of inflammatory cytokine genes. In addition, the effect of melatonin treatment on OBs and OCs was phenocopied by blocking Erk signaling. Taken together, these results suggest that melatonin suppresses the early differentiation of both OBs and OCs through inhibition of epidermal Erk signaling in the fractured scale.

The physiologic effect of melatonin to bone homeostasis has recently entered the spotlight. Many studies working on mammalian mesenchymal cell lines showed melatonin can promote OB differentiation via activation of the ERK1/2-RUNX2 pathway (Sethi et al., 2010; Park et al., 2011; Maria and Witt-Enderby, 2014). Some research on the effect of melatonin for osteoclastogenesis using murine RAW 264.7 cells demonstrated melatonin alters RANKL/OPG ratio to inhibit OC differentiation (Koyama et al., 2002; Amstrup et al., 2013). It is also reported that melatonin inhibits the RANKL-mediated NF-kB activation to repress the differentiation of bone marrow-derived macrophages into OCs (Kim et al., 2017). Thus, in vitro studies of mammalian cells showed beneficial effects of melatonin on bone metabolism as well as antiresorptive

effects, while the effects of melatonin on fracture healing in vivo have not yet been clearly shown in mammals. Despite the importance of cell-cell interaction between OBs and OCs in bone metabolism, the proliferative effect of melatonin on OBs has been investigated using OB monocultures in most reports. Indeed, an inhibitory effect of melatonin on OBs has been shown when OBs were co-cultured with OCs and other types of cells in bone tissue (Suzuki et al., 2002). The data shown in this chapter also suggest that melatonin suppresses both OB and OC differentiation in the early steps of fracture healing. While age-related reduction in melatonin is considered to result in bone loss and osteoporosis (Li et al., 2019), excessive melatonin treatment may inhibit fracture healing.

Major actions of melatonin are mediated by specific membrane receptors, MT1 and MT2 (Histing et al., 2012; Park et al., 2011; Satomura et al., 2007), which belong to the G-protein coupled receptor family. Six melatonin receptor genes have been identified in the zebrafish genome as a homolog to those found in mammals, amphibians or birds (Shang and Zhdanova, 2007). However, the expression of these receptor genes was detected in epithelial cells, but not in OBs and OCs, in the fractured scale. Since enhanced Erk signaling in epidermal cells of fractured scales was repressed by melatonin treatment, it is likely that the main receivers of melatonin in the zebrafish scale are epidermal cells, and that Erk1/2 is one of the key regulatory pathways involved in OB differentiation in the zebrafish scale, as has been shown in mammals (Ge et al., 2007; Matsushita et al., 2009). Iwasaki et al. showed that epidermal cells in the zebrafish scale promote OB proliferation and bone morphogenesis through Sonic hedgehog (Shh) signaling (Iwasaki et al., 2018), suggesting that bone morphogenesis is supported by epidermal cells. Although further studies are needed to precisely determine the role of melatonin in bone morphogenesis, melatonin may negatively affect environmental "niches" that promote

OB and OC differentiation in the bone tissue.
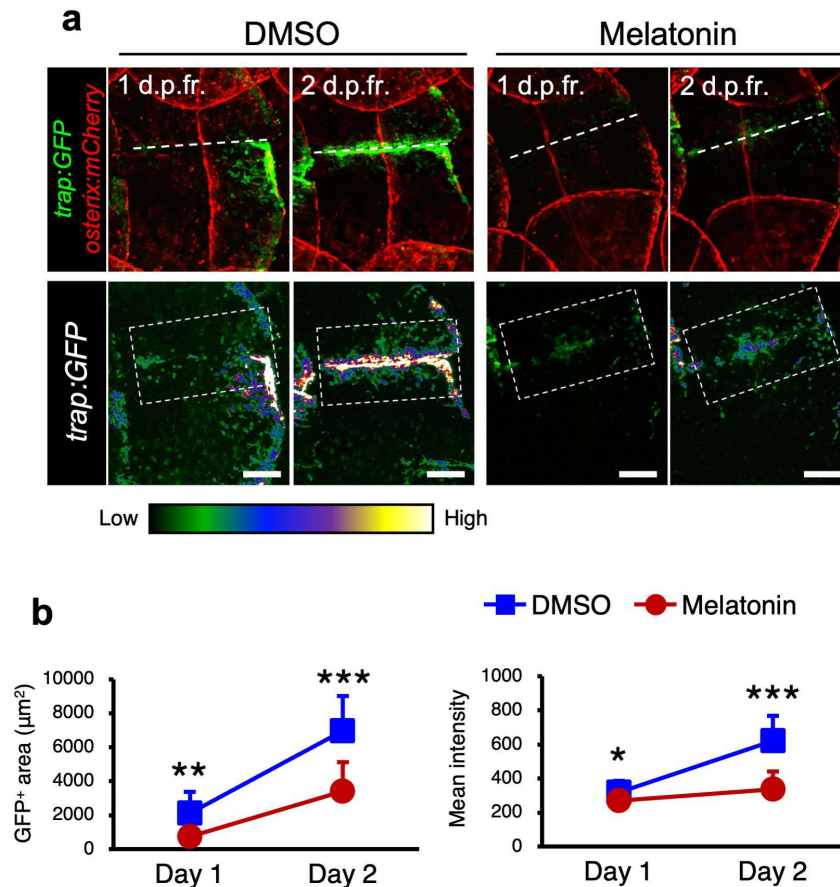
Figure 4.1 Melatonin represses the convergence of *trap:GFP⁺* OCs at the fracture site.

(**a**) Representative confocal images of a fractured scale in *trap:GFP*; *osterix:mCherry* double-transgenic zebrafish treated with DMSO or melatonin at 1 or 2 d.p.fr. Upper panels show the expression of *trap:GFP* (green) and *osterix:mCherry* (red), and lower panels show a heat spectrum of *trap:GFP* expression. Dotted lines in upper panels show the fracture site. Dotted squares in lower panels show the area where the mean intensity of GFP was measured. Images are orientated with the anterior side to the left and the dorsal side to the top. (**b**) The coverage area of *trap:GFP⁺* cells (upper) and mean intensity (lower) of GFP in the fractured scale of DMSO (n = 9) or melatonin-treated zebrafish (n = 8). bars, 200 μm; *$p < 0.05$; **$p < 0.01$; ***$p < 0.001$ by Student's t-test; error bars, s.d.
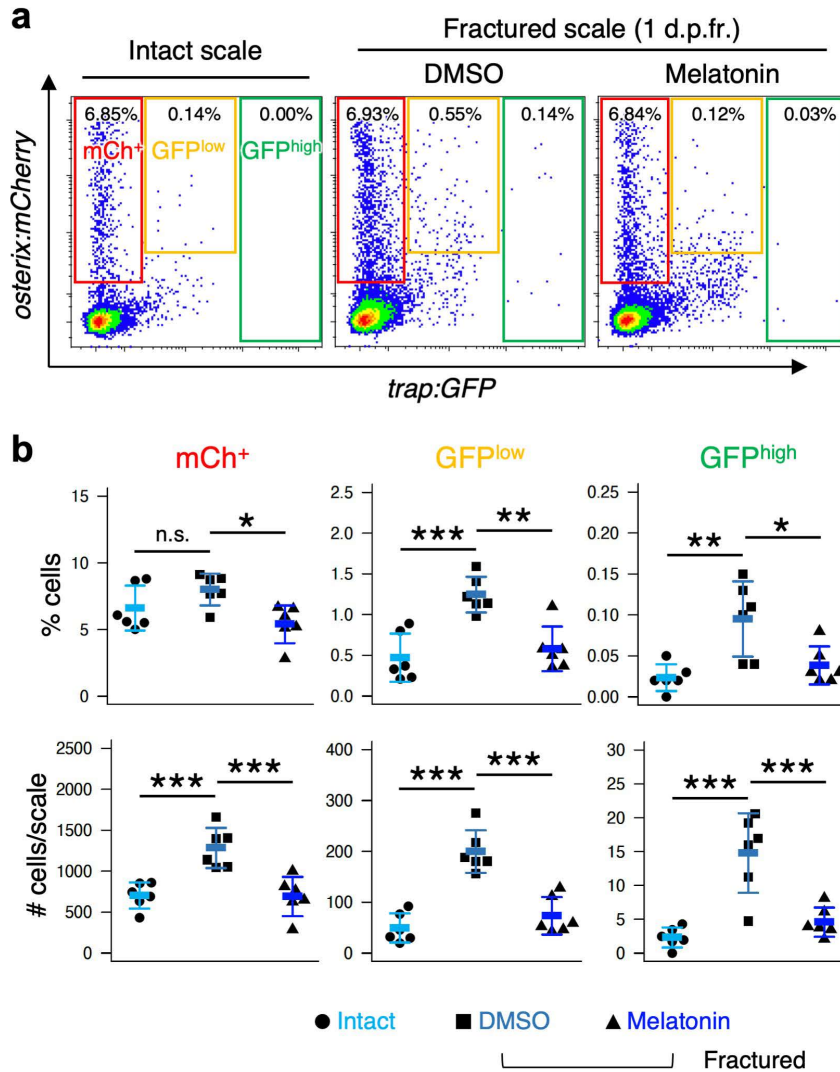
Figure 4.2 Treatment of melatonin reduces the number of OBs and OCs in the fractured scale.

(**a**) Representative FCM results of cells from intact scales or fractured scales of DMSO- or melatonin-treated zebrafish at 1 d.p.fr. The gate of mCh+, GFPlow, and GFPhigh shows *trap:GFP⁻ osterix:mCherry⁺*, *trap:GFPlow osterix:mCherry⁺*, and *trap:GFPhigh* cells, respectively. (**b**) The percentage and absolute number of mCh+, GFPlow, and GFPhigh cells in an intact or fractured scale of DMSO or melatonin-treated zebrafish at 1 d.p.fr. (n = 6 for each group). *$p < 0.05$; **$p < 0.01$; ***$p < 0.001$ by one-way ANOVA followed by Dunnett's test; error bars, s.d.; n.s., no significance.
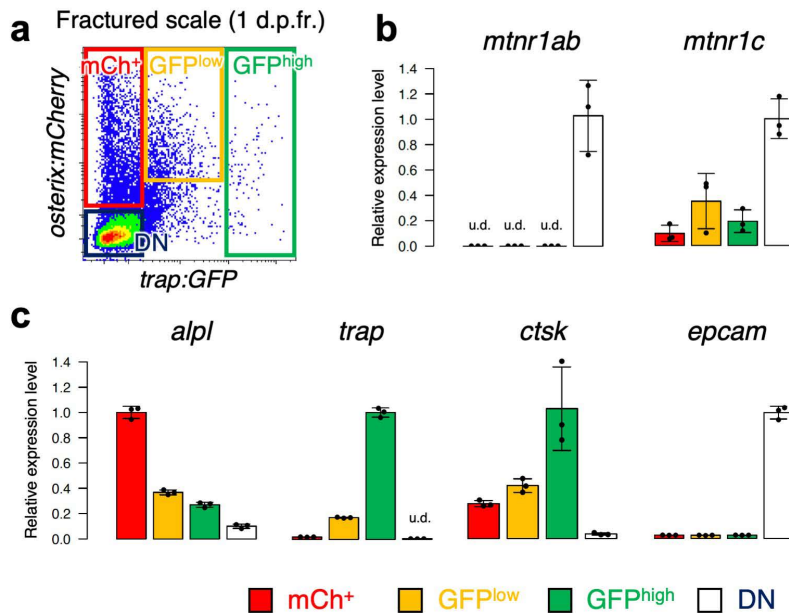
Figure 4.3 Epithelial cells express melatonin receptor genes in the scale.

(**a**) Cells in the mCh⁺, GFPlow, GFPhigh, and double-negative (DN) fraction were isolated from fractured scales at 1 d.p.fr. (**b**) Expression levels of melatonin receptor genes, *mtnr1ab* and *mtnr1c*, in each fraction. (**c**) Expression levels of *alpl*, *trap*, *ctsk*, and *epcam* in each fraction. Error bars, s.d. (n = 3 for each); u.d., undetected.
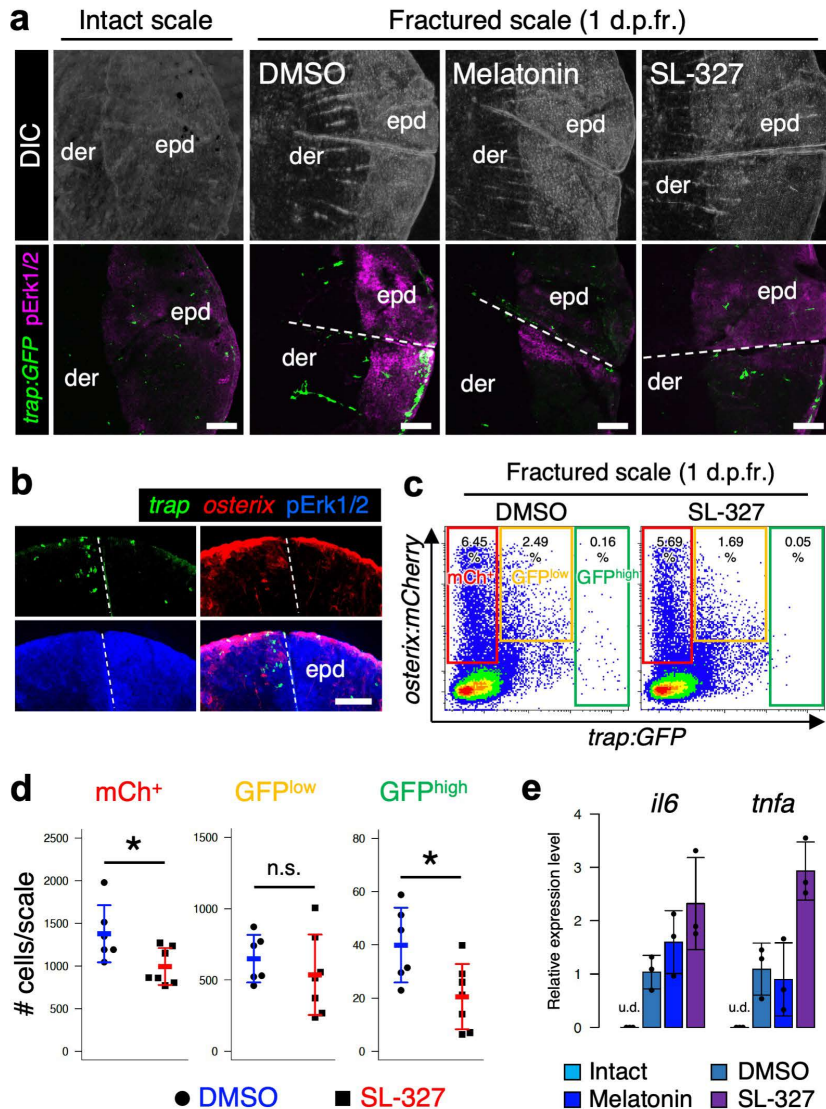
Figure 4.4 Melatonin suppresses epidermal Erk signaling in the fractured scale.

(**a**) Immunohistochemistry with anti-pErk1/2 antibodies in an intact or fractured scale from DMSO-, melatonin-, or SL-327-treated zebrafish at 1 d.p.fr. Upper panels show an image of the differential interference contrast (DIC) and lower panels show a merged image of *trap:GFP* and pErk1/2. (**b**) Immunohistochemistry in the epidermal area of a fractured scale from *trap:GFP*; *osterix:mCherry* double-transgenic zebrafish at 1 d.p.fr. Dotted lines indicate the fractured site. (**c**) Representative FCM results of cells from fractured scales of DMSO- or SL-327-treated zebrafish. (**d**) The absolute number of mCh+, GFPlow, and GFPhigh cells in a fractured scale of DMSO- (n = 6) or SL-327-treated zebrafish (n = 7 for each) at 1 d.p.fr. (**e**) Expression levels of *il6* and *tnfa* in the intact scale or fractured scale of zebrafish treated with DMSO, melatonin, or SL-327 (n = 3 for each). Scale bars, 200 μm; *$p < 0.05$ by Student's t-test; error bars, s.d; der, dermis; epd, epidermis; n.s., no significance; u.d., undetected.

Chapter 5

General discussion

The skeleton is maintained by successive and balanced absorbance and formation of bone tissue through life. OCs are the only cell that can resorb mineralized bone tissue, whereas OBs are responsible for bone formation (Chen et al., 2018). Overactivation of OCs leads to bone loss (e.g. osteoporosis), while deficiency of OCs causes hematopoietic disorders and osteopetrosis. Besides, OCs also facilitate caner metastasis to the bone (Maurizi and Rucci, 2018). Therefore, understanding how OCs are regulated in vivo is crucial for developing therapies for bone disorders.

There are several stages for maturation of OCs from myeloid precursors, which can potentially differentiate into monocytes/macrophages and granulocytes: (1) Myeloid precursors acquired with OC differentiation signals (MCSF and RANKL) become OC precursors, which express TRAP and calcitonin receptors. (2) OC precursors fuse to generate a multinucleated OC. (3) multinucleated OCs are polarized and get mature to resorb bone matrix. RANK/RANKL signaling is pivotal for osteoclatogenesis. Both RANK- and RANKL-deficient mice show a severe osteopetrotic phenotype, caused by failure in OC formation (Kong et al., 1999; Li et al., 2000). RANKL is mainly produced by OBs, stromal cells, and osteocytes in the bone tissue. Activation of RANK/RANKL signaling induces the recruitment of TRAF6, leading to the translocation of NF-kB into the nucleus to activate the transcription of downstream target genes, which are essential for OC differentiation (Li et al., 2000; Chen et al., 2018; Cappariello et al., 2014). These signal networks involved in osteoclastogenesis have been studied in vitro since 1990s. Due to many difficulties, however, studies of OC differentiation in vivo were limited to conventional histological evaluation, which is the 'static' analysis of cell morphology and molecular expression on histological sections (Hashimoto et al., 2020). Recently, a novel intravital imaging system for bone tissue has been established in the mouse model (Ishii

et al, 2009). However, the penetration depth in two-photon microscopy is up to 800-1000 μm in soft tissues and 200 μm in hard tissues (e.g. bone) (Hashimoto et al., 2020), indicating limitation of applied areas in bone tissue.

Recently, the zebrafish is gaining popularity in the field of disease and regeneration research of bone tissue, owing high similarities with mammalian bone tissue. The zebrafish scale has some unique features for bone research: it has a thin and simple structure located on the body-surface with high regenerative capacity, enabling in vivo imaging of bone regeneration using fluorescently labeled transgenic zebrafish. In addition, since a number of scales can be obtained simultaneously from a zebrafish, it is also possible to perform high-throughput examination using zebrafish scales (Mariotti et al., 2015; Witten et al., 2017). It should also be noted that OBs and OCs in the scale are highly similar with their mammalian counterparts in terms of morphology, gene expression, and functions (Renn et al., 2006; Sire and Akimenko, 2004; Sire et al., 1997; Suzuki and Hattori, 2002). Thus, the zebrafish scale is a suitable model to figure out the regulatory mechanisms of OC differentiation.

In vivo imaging of fractured scales in a double-transgenic zebrafish, *trap:GFP*; *osterix:mCherry*, revealed that *trap:GFP$^+$* OCs converged at the fractured site during the early stage of the healing process. Morphological analysis showed that GFP^{high} cells have a typical feature of OCs, including multiple nuclei, numerous mitochondria, and a compact Golgi apparatus located near the nucleus. The gene expression pattern of GFP^{high} cells also showed a representative feature of OCs, including the high expression level of *rank*, *trap*, *nfatc1*, and *ctsk*. In contrast, morphological and expression analysis revealed that GFP^{low} cells possess representative features of OC precursors, which includes monocyte/macrophages and myeloid precursors. Live-imaging analysis also provided

evidence that small round *trap:GFP*^{+} cells fused to generate a multinucleated OC, which is larger in size and brighter in GFP expression compared to unfused cells. Although further characterization is needed to determine differentiation stages of OCs, GFP[low] and GFP^{high} cells can be used to isolate different stages of OCs from fractured scales.

EVs are secreted by nearly all types of cells and widely distributed in the tissues and body fluid, ranging from 30 nm to 1000nm in diameter, of which characters have been highly conserved throughout evolution (Tao and Guo 2019). Since EVs carry various contents (proteins, mRNAs, microRNAs, lipids etc.), EVs derived from OCs and OBs are considered as an important player to regulate bone homeostasis. Transplantation assays in transgenic zebrafish confirmed that the mCherry[+] particles observed in the cytoplasm of *trap:GFP*[+] OCs are due to the uptake of OB-derived EVs. RNA-seq analysis revealed that OB-derived EVs abundantly contain signaling molecules and miRNAs. In vitro co-culture experiments showed that these EVs promote OC differentiation via Rankl-dependent manner. Interestingly induced *trap:GFP*[+] OCs in the co-culture experiment also contained mCherry[+] EVs, similar with OCs observed in the fractured scale. Importantly, time-lapse imaging of a fractured scale in a *trap:GFP*; *osterix:mCherry* zebrafish captured the moment that OCs engulf OB-derived EVs prior to convergence at the fracture site. Taken together, the zebrafish scale model enables us to image and isolate OCs and OBs in order to perform various experiments, including tracing the dynamics of these cells in vivo at every stage of fracture healing.

Crisper/Cas9-based gene knockdown technique is useful to seek the key molecules involved OC differentiation and EVs-mediated intracellular communication. To examine the role of Rankl in OCs differentiation, four gRNAs were designed and injected into *trap:GFP*; *osterix:mCherry* zebrafish embryos. The *rankl* gRNA-injected zebrafish

partially survived to adulthood, but showed severe body curvature. The number of *trap:GFP*[+] OCs was significantly reduced in the fractured scales of *rankl* gRNA-injected zebrafish. Moreover, OB-derived EVs from *rankl* gRNA-injected zebrafish failed to induce OC differentiation in vitro. Collectively, these data suggest that Rankl signaling in OBs-derived EVs facilitates OC differentiation.

The zebrafish scale model is also useful to examine the function of hormones and chemical compounds. PTH treatment enhanced the activation of both OBs and OCs in the fractured scale, as has been shown in mammals (Furuya et al., 2018; Tu et al., 2018). It could be expected that the effect of melatonin on OCs and OBs in zebrafish also similar with those in mammals: melatonin represses OCs but activates OBs (Satomura et al., 2007; Park et al., 2011; Li et al., 2019). However, both OBs and OCs in the fractured scale of melatonin-treated zebrafish were reduced compared with control zebrafish. The inhibitory effect of melatonin on OBs and OCs in the fractured scale is caused by blocking epidermal ERK signaling, which is enhanced by fracture stress. Further studies are needed to determine the molecular mechanisms of epidermal Erk signaling in the regulation of OBs and OCs.

There are still some unknown things that needed to be determined by future works. For instance, the site of OC differentiation in the fractured scale is still unknown. In mammals, OC precursors generated in the bone marrow circulate in blood and migrate to the bone surface, where they differentiate, fuse, and get maturation. In contrast, hematopoietic stem cells in teleost fish are mainly present in the kidney. Although cell fusion of OCs were observed in the fractured scale, it is still unclear whether OC precursors are generated in the kidney or scale. In addition, the molecular mechanisms underlying migration of OC precursors to the fracture site also remain to be elusive. It is also

important to investigate the function of miRNAs within OB-derived EVs because miRNAs in EVs can potentially regulate gene expression in the EV-receiving cell. Due to the risk of side effects, the usage of some medications for osteoporosis and other bone disorders is limited. Developing therapeutic capsules by modifying EVs may be effective to treat bone disorders. The zebrafish scale model is helpful to modify EVs since OB-derived EVs can be isolated by flow cytometry. It also remains to be elusive why *rankl* gRNA-injected zebrafish showed severe body curvature at around one month old, which is similar with adolescent idiopathic scoliosis. Generation of a *rankl* mutant zebrafish line may be useful to explore the molecular and cellular mechanisms underlying scoliosis.

In conclusion, the zebrafish scale, in combination with intubation anesthesia, enables live-imaging of OBs and OCs in vivo during fracture healing. In addition, cell sorting by flow cytometry from the scale makes it possible to examine gene expression and perform cell culture assays for each cell type. This model is particularly useful for examining the function of genes, chemical compounds, or hormones in the activity of OBs and OCs. Although it should be appreciated not all observations from zebrafish are translatable to the human conditions, zebrafish fractured scale model can make a valuable contribution towards a better understanding of the regulatory mechanisms of bone resorption and formation and developing new therapeutics.

References

Amarasekara, D.S., Yun, H., Kim, S., Lee, N., Kim, H., and Rho, J. (2018). Regulation of Osteoclast Differentiation by Cytokine Networks. Immune Netw 18, e8. 10.4110/in.2018.18.e8.

Arnett, T.R., and Orriss, I.R. (2018). Metabolic properties of the osteoclast. Bone 115, 25-30. 10.1016/j.bone.2017.12.021.

Bahney, C.S., Zondervan, R.L., Allison, P., Theologis, A., Ashley, J.W., Ahn, J., Miclau, T., Marcucio, R.S., and Hankenson, K.D. (2019). Cellular biology of fracture healing. J Orthop Res 37, 35-50. 10.1002/jor.24170.

Baht, G.S., Vi, L., and Alman, B.A. (2018). The Role of the Immune Cells in Fracture Healing. Curr Osteoporos Rep 16, 138-145. 10.1007/s11914-018-0423-2.

Ban, Z.N., Li, Z.J., Gu, Q.S., Cheng, J., Huang, Q., and Xing, S.X. (2019). Correlation of serum PTH level and fracture healing speed in elderly patients with hip fracture. J Orthop Surg Res 14, 361. 10.1186/s13018-019-1413-5.

Bar-Shavit, Z. (2007). The osteoclast: a multinucleated, hematopoietic-origin, bone-resorbing osteoimmune cell. J Cell Biochem 102, 1130-1139. 10.1002/jcb.21553.

Baron, R., Neff, L., Tran Van, P., Nefussi, J.R., and Vignery, A. (1986). Kinetic and cytochemical identification of osteoclast precursors and their differentiation into multinucleated osteoclasts. Am J Pathol 122, 363-378.

Beil, F.T., Barvencik, F., Gebauer, M., Seitz, S., Rueger, J.M., Ignatius, A., Pogoda, P., Schinke, T., and Amling, M. (2010). Effects of estrogen on fracture healing in mice. J Trauma 69, 1259-1265. 10.1097/TA.0b013e3181c4544d.

Bergen, D.J.M., Kague, E., and Hammond, C.L. (2019). Zebrafish as an Emerging Model for Osteoporosis: A Primary Testing Platform for Screening New Osteo-Active

Compounds. Front Endocrinol (Lausanne) 10, 6. 10.3389/fendo.2019.00006.

Bird, N.C., and Mabee, P.M. (2003). Developmental morphology of the axial skeleton of the zebrafish, Danio rerio (Ostariophysi: Cyprinidae). Dev Dyn 228, 337-357. 10.1002/dvdy.10387.

Blum, N., and Begemann, G. (2015). Osteoblast de- and redifferentiation are controlled by a dynamic response to retinoic acid during zebrafish fin regeneration. Development 142, 2894-2903. 10.1242/dev.120204.

Boyce, B.F. (2013). Advances in the regulation of osteoclasts and osteoclast functions. J Dent Res 92, 860-867. 10.1177/0022034513500306.

Boyle, W.J., Simonet, W.S., and Lacey, D.L. (2003). Osteoclast differentiation and activation. Nature 423, 337-342. 10.1038/nature01658.

Budai, Z., Ujlaky-Nagy, L., Kis, G.N., Antal, M., Bankó, C., Bacsó, Z., Szondy, Z., and Sarang, Z. (2019). Macrophages engulf apoptotic and primary necrotic thymocytes through similar phosphatidylserine-dependent mechanisms. FEBS Open Bio 9, 446-456. 10.1002/2211-5463.12584.

Cappariello, A., Loftus, A., Muraca, M., Maurizi, A., Rucci, N., and Teti, A. (2018). Osteoblast-Derived Extracellular Vesicles Are Biological Tools for the Delivery of Active Molecules to Bone. Journal of Bone and Mineral Research 33, 517-533. 10.1002/jbmr.3332.

Cappariello, A., Maurizi, A., Veeriah, V., and Teti, A. (2014). The Great Beauty of the osteoclast. Arch Biochem Biophys 558, 70-78. 10.1016/j.abb.2014.06.017.

Caraguel, F., Bessonov, N., Demongeot, J., Dhouailly, D., and Volpert, V. (2016). Wound Healing and Scale Modelling in Zebrafish. Acta Biotheor 64, 343-358. 10.1007/s10441-016-9298-8.

Cardinali, D.P., Ladizesky, M.G., Boggio, V., Cutrera, R.A., and Mautalen, C. (2003). Melatonin effects on bone: experimental facts and clinical perspectives. J Pineal Res 34, 81-87. 10.1034/j.1600-079x.2003.00028.x.

Carnovali, M., Luzi, L., Banfi, G., and Mariotti, M. (2016). Chronic hyperglycemia affects bone metabolism in adult zebrafish scale model. Endocrine 54, 808-817. 10.1007/s12020-016-1106-3.

Caruso, S., and Poon, I.K.H. (2018). Apoptotic Cell-Derived Extracellular Vesicles: More Than Just Debris. Front Immunol 9, 1486. 10.3389/fimmu.2018.01486.

Chatani, M., Takano, Y., and Kudo, A. (2011). Osteoclasts in bone modeling, as revealed by in vivo imaging, are essential for organogenesis in fish. Dev Biol 360, 96-109. 10.1016/j.ydbio.2011.09.013.

Chen, X., Wang, Z.Q., Duan, N., Zhu, G.Y., Schwarz, E.M., and Xie, C. (2018). Osteoblast-osteoclast interactions. Connective Tissue Research 59, 99-107. 10.1080/03008207.2017.1290085.

Crockett, J.C., Rogers, M.J., Coxon, F.P., Hocking, L.J., and Helfrich, M.H. (2011). Bone remodelling at a glance. J Cell Sci 124, 991-998. 10.1242/jcs.063032.

de Jong, J.L., Burns, C.E., Chen, A.T., Pugach, E., Mayhall, E.A., Smith, A.C., Feldman, H.A., Zhou, Y., and Zon, L.I. (2011). Characterization of immune-matched hematopoietic transplantation in zebrafish. Blood 117, 4234-4242. 10.1182/blood-2010-09-307488.

de Vrieze, E., Sharif, F., Metz, J.R., Flik, G., and Richardson, M.K. (2011). Matrix metalloproteinases in osteoclasts of ontogenetic and regenerating zebrafish scales. Bone 48, 704-712. 10.1016/j.bone.2010.12.017.

de Vrieze, E., Zethof, J., Schulte-Merker, S., Flik, G., and Metz, J.R. (2015). Identification

of novel osteogenic compounds by an ex-vivo sp7:luciferase zebrafish scale assay. Bone 74, 106-113. 10.1016/j.bone.2015.01.006.

Deng, L., Peng, Y., Jiang, Y., Wu, Y., Ding, Y., Wang, Y., Xu, D., and Fu, Q. (2017). Imipramine Protects against Bone Loss by Inhibition of Osteoblast-Derived Microvesicles. Int J Mol Sci 18. 10.3390/ijms18051013.

Deng, L., Wang, Y., Peng, Y., Wu, Y., Ding, Y., Jiang, Y., Shen, Z., and Fu, Q. (2015). Osteoblast-derived microvesicles: A novel mechanism for communication between osteoblasts and osteoclasts. Bone 79, 37-42. 10.1016/j.bone.2015.05.022.

Dietrich, K., Fiedler, I.A., Kurzyukova, A., López-Delgado, A.C., McGowan, L.M., Geurtzen, K., Hammond, C.L., Busse, B., and Knopf, F. (2021). Skeletal Biology and Disease Modeling in Zebrafish. J Bone Miner Res 36, 436-458. 10.1002/jbmr.4256.

Dimitriou, R., Jones, E., McGonagle, D., and Giannoudis, P.V. (2011). Bone regeneration: current concepts and future directions. BMC Med 9, 66. 10.1186/1741-7015-9-66.

Drissi, H., and Sanjay, A. (2016). The Multifaceted Osteoclast; Far and Beyond Bone Resorption. J Cell Biochem 117, 1753-1756. 10.1002/jcb.25560.

Egermann, M., Goldhahn, J., and Schneider, E. (2005). Animal models for fracture treatment in osteoporosis. Osteoporos Int 16 Suppl 2, S129-138. 10.1007/s00198-005-1859-7.

Einhorn, T.A., and Gerstenfeld, L.C. (2015). Fracture healing: mechanisms and interventions. Nat Rev Rheumatol 11, 45-54. 10.1038/nrrheum.2014.164.

EL Andaloussi, S., Mäger, I., Breakefield, X.O., and Wood, M.J. (2013). Extracellular vesicles: biology and emerging therapeutic opportunities. Nat Rev Drug Discov 12, 347-357. 10.1038/nrd3978.

Franco, N.H., and Olsson, I.A. (2014). Scientists and the 3Rs: attitudes to animal use in biomedical research and the effect of mandatory training in laboratory animal science. Lab Anim 48, 50-60. 10.1177/0023677213498717.

Furuya, M., Kikuta, J., Fujimori, S., Seno, S., Maeda, H., Shirazaki, M., Uenaka, M., Mizuno, H., Iwamoto, Y., Morimoto, A., et al. (2018). Direct cell-cell contact between mature osteoblasts and osteoclasts dynamically controls their functions in vivo. Nature Communications 9, 300. 10.1038/s41467-017-02541-w.

Ge, C., Xiao, G., Jiang, D., and Franceschi, R.T. (2007). Critical role of the extracellular signal-regulated kinase-MAPK pathway in osteoblast differentiation and skeletal development. J Cell Biol 176, 709-718. 10.1083/jcb.200610046.

Ge, M., Ke, R., Cai, T., Yang, J., and Mu, X. (2015). Identification and proteomic analysis of osteoblast-derived exosomes. Biochem Biophys Res Commun 467, 27-32. 10.1016/j.bbrc.2015.09.135.

Geurtzen, K., Knopf, F., Wehner, D., Huitema, L.F., Schulte-Merker, S., and Weidinger, G. (2014). Mature osteoblasts dedifferentiate in response to traumatic bone injury in the zebrafish fin and skull. Development 141, 2225-2234. 10.1242/dev.105817.

Gibbings, D.J., Ciaudo, C., Erhardt, M., and Voinnet, O. (2009). Multivesicular bodies associate with components of miRNA effector complexes and modulate miRNA activity. Nat Cell Biol 11, 1143-1149. 10.1038/ncb1929.

Gomes, P.S., and Fernandes, M.H. (2011). Rodent models in bone-related research: the relevance of calvarial defects in the assessment of bone regeneration strategies. Lab Anim 45, 14-24. 10.1258/la.2010.010085.

Gomez Perdiguero, E., Klapproth, K., Schulz, C., Busch, K., Azzoni, E., Crozet, L., Garner, H., Trouillet, C., de Bruijn, M.F., Geissmann, F., and Rodewald, H.R.

(2015). Tissue-resident macrophages originate from yolk-sac-derived erythro-myeloid progenitors. Nature 518, 547-551. 10.1038/nature13989.

Haffner-Luntzer, M., Kovtun, A., Rapp, A.E., and Ignatius, A. (2016). Mouse Models in Bone Fracture Healing Research.

Han, Y., You, X., Xing, W., Zhang, Z., and Zou, W. (2018). Paracrine and endocrine actions of bone-the functions of secretory proteins from osteoblasts, osteocytes, and osteoclasts. Bone Res 6, 16. 10.1038/s41413-018-0019-6.

Hayman, A.R. (2008). Tartrate-resistant acid phosphatase (TRAP) and the osteoclast/immune cell dichotomy. Autoimmunity 41, 218-223. 10.1080/08916930701694667.

Hayman, A.R., Jones, S.J., Boyde, A., Foster, D., Colledge, W.H., Carlton, M.B., Evans, M.J., and Cox, T.M. (1996). Mice lacking tartrate-resistant acid phosphatase (Acp 5) have disrupted endochondral ossification and mild osteopetrosis. Development 122, 3151-3162.

Heino, T.J., and Hentunen, T.A. (2008). Differentiation of osteoblasts and osteocytes from mesenchymal stem cells. Curr Stem Cell Res Ther 3, 131-145.

Histing, T., Anton, C., Scheuer, C., Garcia, P., Holstein, J.H., Klein, M., Matthys, R., Pohlemann, T., and Menger, M.D. (2012). Melatonin impairs fracture healing by suppressing RANKL-mediated bone remodeling. J Surg Res 173, 83-90. 10.1016/j.jss.2010.08.036.

Histing, T., Kuntz, S., Stenger, D., Scheuer, C., Garcia, P., Holstein, J.H., Klein, M., Pohlemann, T., and Menger, M.D. (2013). Delayed fracture healing in aged senescence-accelerated P6 mice. J Invest Surg 26, 30-35. 10.3109/08941939.2012.687435.

Holzapfel, B.M., Wagner, F., Loessner, D., Holzapfel, N.P., Thibaudeau, L., Crawford, R., Ling, M.T., Clements, J.A., Russell, P.J., and Hutmacher, D.W. (2014). Species-specific homing mechanisms of human prostate cancer metastasis in tissue engineered bone. Biomaterials 35, 4108-4115. 10.1016/j.biomaterials.2014.01.062.

Ikegame, M., Hattori, A., Tabata, M.J., Kitamura, K.I., Tabuchi, Y., Furusawa, Y., Maruyama, Y., Yamamoto, T., Sekiguchi, T., Matsuoka, R., et al. (2019). Melatonin is a potential drug for the prevention of bone loss during space flight. J Pineal Res 67, e12594. 10.1111/jpi.12594.

Ishii, M., Egen, J.G., Klauschen, F., Meier-Schellersheim, M., Saeki, Y., Vacher, J., Proia, R.L., and Germain, R.N. (2009). Sphingosine-1-phosphate mobilizes osteoclast precursors and regulates bone homeostasis. Nature 458, 524-528. 10.1038/nature07713.

Iwasaki, M., Kuroda, J., Kawakami, K., and Wada, H. (2018). Epidermal regulation of bone morphogenesis through the development and regeneration of osteoblasts in the zebrafish scale. Dev Biol 437, 105-119. 10.1016/j.ydbio.2018.03.005.

Jacome-Galarza, C.E., Percin, G.I., Muller, J.T., Mass, E., Lazarov, T., Eitler, J., Rauner, M., Yadav, V.K., Crozet, L., Bohm, M., et al. (2019). Developmental origin, functional maintenance and genetic rescue of osteoclasts. Nature 568, 541-545. 10.1038/s41586-019-1105-7.

Kalra, H., Drummen, G.P., and Mathivanan, S. (2016). Focus on Extracellular Vesicles: Introducing the Next Small Big Thing. Int J Mol Sci 17, 170. 10.3390/ijms17020170.

Kikuta, J., Wada, Y., Kowada, T., Wang, Z., Sun-Wada, G.H., Nishiyama, I., Mizukami, S., Maiya, N., Yasuda, H., Kumanogoh, A., et al. (2013). Dynamic visualization of

RANKL and Th17-mediated osteoclast function. J Clin Invest 123, 866-873. 10.1172/JCI65054.

Kim, H.J., Bae, M.K., and Kim, Y.D. (2017). Suppression of Osteoclastogenesis by Melatonin: A Melatonin Receptor-Independent Action. Int J Mol Sci 18. 10.3390/ijms18061142.

Kobayashi, I., Kobayashi-Sun, J., Hirakawa, Y., Ouchi, M., Yasuda, K., Kamei, H., Fukuhara, S., and Yamaguchi, M. (2020). Dual role of Jam3b in early hematopoietic and vascular development. Development 147. 10.1242/dev.181040.

Kobayashi, I., Kobayashi-Sun, J., Kim, A.D., Pouget, C., Fujita, N., Suda, T., and Traver, D. (2014). Jam1a-Jam2a interactions regulate haematopoietic stem cell fate through Notch signalling. Nature 512, 319-323. 10.1038/nature13623.

Kobayashi, I., Kondo, M., Yamamori, S., Kobayashi-Sun, J., Taniguchi, M., Kanemaru, K., Katakura, F., and Traver, D. (2019). Enrichment of hematopoietic stem/progenitor cells in the zebrafish kidney. Sci Rep 9, 14205. 10.1038/s41598-019-50672-5.

Kobayashi-Sun, J., Yamamori, S., Kondo, M., Kuroda, J., Ikegame, M., Suzuki, N., Kitamura, K.I., Hattori, A., Yamaguchi, M., and Kobayashi, I. (2020). Uptake of osteoblast-derived extracellular vesicles promotes the differentiation of osteoclasts in the zebrafish scale. Commun Biol 3, 190. 10.1038/s42003-020-0925-1.

Kong, Y.Y., Yoshida, H., Sarosi, I., Tan, H.L., Timms, E., Capparelli, C., Morony, S., Oliveira-dos-Santos, A.J., Van, G., Itie, A., et al. (1999). OPGL is a key regulator of osteoclastogenesis, lymphocyte development and lymph-node organogenesis. Nature 397, 315-323. 10.1038/16852.

Koyama, H., Nakade, O., Takada, Y., Kaku, T., and Lau, K.H. (2002). Melatonin at

pharmacologic doses increases bone mass by suppressing resorption through down-regulation of the RANKL-mediated osteoclast formation and activation. J Bone Miner Res 17, 1219-1229. 10.1359/jbmr.2002.17.7.1219.

Lacey, D.L., Timms, E., Tan, H.L., Kelley, M.J., Dunstan, C.R., Burgess, T., Elliott, R., Colombero, A., Elliott, G., Scully, S., et al. (1998). Osteoprotegerin ligand is a cytokine that regulates osteoclast differentiation and activation. Cell 93, 165-176. 10.1016/s0092-8674(00)81569-x.

Ladizesky, M.G., Boggio, V., Albornoz, L.E., Castrillón, P.O., Mautalen, C., and Cardinali, D.P. (2003). Melatonin increases oestradiol-induced bone formation in ovariectomized rats. J Pineal Res 34, 143-151. 10.1034/j.1600-079x.2003.00021.x.

Ladizesky, M.G., Cutrera, R.A., Boggio, V., Somoza, J., Centrella, J.M., Mautalen, C., and Cardinali, D.P. (2001). Effect of melatonin on bone metabolism in ovariectomized rats. Life Sci 70, 557-565. 10.1016/s0024-3205(01)01431-x.

Li, J., Sarosi, I., Yan, X.Q., Morony, S., Capparelli, C., Tan, H.L., McCabe, S., Elliott, R., Scully, S., Van, G., et al. (2000). RANK is the intrinsic hematopoietic cell surface receptor that controls osteoclastogenesis and regulation of bone mass and calcium metabolism. Proc Natl Acad Sci U S A 97, 1566-1571. 10.1073/pnas.97.4.1566.

Li, T., Jiang, S., Lu, C., Yang, W., Yang, Z., Hu, W., Xin, Z., and Yang, Y. (2019). Melatonin: Another avenue for treating osteoporosis? J Pineal Res 66, e12548. 10.1111/jpi.12548.

Li, W., Wang, K., Liu, Z., and Ding, W. (2015). HIF-1α change in serum and callus during fracture healing in ovariectomized mice. Int J Clin Exp Pathol 8, 117-126.

Liu, L., Xu, Y., Reiter, R.J., Pan, Y., Chen, D., Liu, Y., Pu, X., Jiang, L., and Li, Z. (2016a). Inhibition of ERK1/2 Signaling Pathway is Involved in Melatonin's

Antiproliferative Effect on Human MG-63 Osteosarcoma Cells. Cell Physiol Biochem 39, 2297-2307. 10.1159/000447922.

Liu, S., Zhu, W., Li, S., Ma, J., Zhang, H., Li, Z., Zhang, L., Zhang, B., Liang, X., and Shi, W. (2016b). Bovine parathyroid hormone enhances osteoclast bone resorption by modulating V-ATPase through PTH1R. Int J Mol Med 37, 284-292. 10.3892/ijmm.2015.2423.

Lleras-Forero, L., Winkler, C., and Schulte-Merker, S. (2020). Zebrafish and medaka as models for biomedical research of bone diseases. Dev Biol 457, 191-205. 10.1016/j.ydbio.2019.07.009.

Maria, S., Samsonraj, R.M., Munmun, F., Glas, J., Silvestros, M., Kotlarczyk, M.P., Rylands, R., Dudakovic, A., van Wijnen, A.J., Enderby, L.T., et al. (2018). Biological effects of melatonin on osteoblast/osteoclast cocultures, bone, and quality of life: Implications of a role for MT2 melatonin receptors, MEK1/2, and MEK5 in melatonin-mediated osteoblastogenesis. J Pineal Res 64. 10.1111/jpi.12465.

Maria, S., and Witt-Enderby, P.A. (2014). Melatonin effects on bone: potential use for the prevention and treatment for osteopenia, osteoporosis, and periodontal disease and for use in bone-grafting procedures. J Pineal Res 56, 115-125. 10.1111/jpi.12116.

Mariotti, M., Carnovali, M., and Banfi, G. (2015). Danio rerio: the Janus of the bone from embryo to scale. Clin Cases Miner Bone Metab 12, 188-194. 10.11138/ccmbm/2015.12.2.188.

Martin, T.J., and Udagawa, N. (1998). Hormonal regulation of osteoclast function. Trends Endocrinol Metab 9, 6-12. 10.1016/s1043-2760(98)00005-8.

Mathias, J.R., Saxena, M.T., and Mumm, J.S. (2012). Advances in zebrafish chemical

screening technologies. Future Med Chem 4, 1811-1822. 10.4155/fmc.12.115.

Mathieu, M., Martin-Jaular, L., Lavieu, G., and Théry, C. (2019). Specificities of secretion and uptake of exosomes and other extracellular vesicles for cell-to-cell communication. Nat Cell Biol 21, 9-17. 10.1038/s41556-018-0250-9.

Matsuo, K., and Irie, N. (2008). Osteoclast-osteoblast communication. Archives of Biochemistry and Biophysics 473, 201-209. 10.1016/j.abb.2008.03.027.

Matsushita, T., Chan, Y.Y., Kawanami, A., Balmes, G., Landreth, G.E., and Murakami, S. (2009). Extracellular signal-regulated kinase 1 (ERK1) and ERK2 play essential roles in osteoblast differentiation and in supporting osteoclastogenesis. Mol Cell Biol 29, 5843-5857. 10.1128/MCB.01549-08.

Maurizi, A., and Rucci, N. (2018). The Osteoclast in Bone Metastasis: Player and Target. Cancers (Basel) 10. 10.3390/cancers10070218.

Miyazawa , K., Torii, Y., Tabuchi, M., Mizuno , M., Yoshizako, M., Minamoto, C., Kawatani, M., Osada, H., Maeda, H., and Goto, S. (2020). Osteoclast Inhibitors for Bone Fracture Healing in Mice with High-Turnover Osteoporosis. Journal of Hard Tissue Biology 29, 255-262.

Morgan, E.F., Mason, Z.D., Bishop, G., Davis, A.D., Wigner, N.A., Gerstenfeld, L.C., and Einhorn, T.A. (2008). Combined effects of recombinant human BMP-7 (rhBMP-7) and parathyroid hormone (1-34) in metaphyseal bone healing. Bone 43, 1031-1038. 10.1016/j.bone.2008.07.251.

Nagasawa, Y., Takei, M., Iwata, M., Nagatsuka, Y., Tsuzuki, H., Imai, K., Imadome, K.I., Fujiwara, S., and Kitamura, N. (2021). Human osteoclastogenesis in Epstein-Barr virus-induced erosive arthritis in humanized NOD/Shi-scid/IL-2Rγnull mice. PLoS One 16, e0249340. 10.1371/journal.pone.0249340.

Nakano, M., Ikegame, M., Igarashi-Migitaka, J., Maruyama, Y., Suzuki, N., and Hattori, A. (2019). Suppressive effect of melatonin on osteoclast function via osteocyte calcitonin. J Endocrinol 242, 13-23. 10.1530/JOE-18-0707.

Nevius, E., Pinho, F., Dhodapkar, M., Jin, H., Nadrah, K., Horowitz, M.C., Kikuta, J., Ishii, M., and Pereira, J.P. (2015). Oxysterols and EBI2 promote osteoclast precursor migration to bone surfaces and regulate bone mass homeostasis. J Exp Med 212, 1931-1946. 10.1084/jem.20150088.

Noh, J.Y., Yang, Y., and Jung, H. (2020). Molecular Mechanisms and Emerging Therapeutics for Osteoporosis. Int J Mol Sci 21. 10.3390/ijms21207623.

Noishiki, C., Yuge, S., Ando, K., Wakayama, Y., Mochizuki, N., Ogawa, R., and Fukuhara, S. (2019). Live imaging of angiogenesis during cutaneous wound healing in adult zebrafish. Angiogenesis 22, 341-354. 10.1007/s10456-018-09660-y.

O'Loughlin, P.F., Morr, S., Bogunovic, L., Kim, A.D., Park, B., and Lane, J.M. (2008). Selection and development of preclinical models in fracture-healing research. J Bone Joint Surg Am 90 Suppl 1, 79-84. 10.2106/JBJS.G.01585.

Ostrowska, Z., Kos-Kudla, B., Marek, B., Kajdaniuk, D., and Ciesielska-Kopacz, N. (2002). The relationship between the daily profile of chosen biochemical markers of bone metabolism and melatonin and other hormone secretion in rats under physiological conditions. Neuro Endocrinol Lett 23, 417-425.

Ostrowska, Z., Kos-Kudla, B., Swietochowska, E., Marek, B., Kajdaniuk, D., and Górski, J. (2001). Assessment of the relationship between dynamic pattern of nighttime levels of melatonin and chosen biochemical markers of bone metabolism in a rat model of postmenopausal osteoporosis. Neuro Endocrinol Lett 22, 129-136.

Park, C.M., Kim, H.M., Kim, D.H., Han, H.J., Noh, H., Jang, J.H., Park, S.H., Chae, H.J.,

Chae, S.W., Ryu, E.K., et al. (2016). Ginsenoside Re Inhibits Osteoclast Differentiation in Mouse Bone Marrow-Derived Macrophages and Zebrafish Scale Model. Mol Cells 39, 855-861. 10.14348/molcells.2016.0111.

Park, K.H., Kang, J.W., Lee, E.M., Kim, J.S., Rhee, Y.H., Kim, M., Jeong, S.J., Park, Y.G., and Kim, S.H. (2011). Melatonin promotes osteoblastic differentiation through the BMP/ERK/Wnt signaling pathways. J Pineal Res 51, 187-194. 10.1111/j.1600-079X.2011.00875.x.

Pasqualetti, S., Banfi, G., and Mariotti, M. (2012). The zebrafish scale as model to study the bone mineralization process. J Mol Histol 43, 589-595. 10.1007/s10735-012-9425-z.

Paul, S., Schindler, S., Giovannone, D., de Millo Terrazzani, A., Mariani, F.V., and Crump, J.G. (2016). Ihha induces hybrid cartilage-bone cells during zebrafish jawbone regeneration. Development 143, 2066-2076. 10.1242/dev.131292.

Phan, Q.T., Tan, W.H., Liu, R., Sundaram, S., Buettner, A., Kneitz, S., Cheong, B., Vyas, H., Mathavan, S., Schartl, M., and Winkler, C. (2020). Cxcl9l and Cxcr3.2 regulate recruitment of osteoclast progenitors to bone matrix in a medaka osteoporosis model. Proc Natl Acad Sci U S A 117, 19276-19286. 10.1073/pnas.2006093117.

Plotkin, L.I. (2014). Apoptotic osteocytes and the control of targeted bone resorption. Curr Osteoporos Rep 12, 121-126. 10.1007/s11914-014-0194-3.

Plotkin, L.I., and Bruzzaniti, A. (2019). Molecular signaling in bone cells: Regulation of cell differentiation and survival. Adv Protein Chem Struct Biol 116, 237-281. 10.1016/bs.apcsb.2019.01.002.

Rafat, A., Mohammadi Roushandeh, A., Alizadeh, A., Hashemi-Firouzi, N., and Golipoor, Z. (2019). Comparison of The Melatonin Preconditioning Efficacy between Bone

Marrow and Adipose-Derived Mesenchymal Stem Cells. Cell J 20, 450-458. 10.22074/cellj.2019.5507.

Raggatt, L.J., and Partridge, N.C. (2010). Cellular and molecular mechanisms of bone remodeling. J Biol Chem 285, 25103-25108. 10.1074/jbc.R109.041087.

Renn, J., Winkler, C., Schartl, M., Fischer, R., and Goerlich, R. (2006). Zebrafish and medaka as models for bone research including implications regarding space-related issues. Protoplasma 229, 209-214. 10.1007/s00709-006-0215-x.

Romero, G., Sneddon, W.B., Yang, Y., Wheeler, D., Blair, H.C., and Friedman, P.A. (2010). Parathyroid hormone receptor directly interacts with dishevelled to regulate beta-Catenin signaling and osteoclastogenesis. J Biol Chem 285, 14756-14763. 10.1074/jbc.M110.102970.

Rosset, P., Deschaseaux, F., and Layrolle, P. (2014). Cell therapy for bone repair. Orthop Traumatol Surg Res 100, S107-112. 10.1016/j.otsr.2013.11.010.

Rutkovskiy, A., Stensløkken, K.O., and Vaage, I.J. (2016). Osteoblast Differentiation at a Glance. Med Sci Monit Basic Res 22, 95-106. 10.12659/msmbr.901142.

Safinia, N., Becker, P.D., Vaikunthanathan, T., Xiao, F., Lechler, R., and Lombardi, G. (2016). Humanized Mice as Preclinical Models in Transplantation. Methods Mol Biol 1371, 177-196. 10.1007/978-1-4939-3139-2_11.

Samsonraj, R.M., Dudakovic, A., Zan, P., Pichurin, O., Cool, S.M., and van Wijnen, A.J. (2017). A Versatile Protocol for Studying Calvarial Bone Defect Healing in a Mouse Model. Tissue Eng Part C Methods 23, 686-693. 10.1089/ten.TEC.2017.0205.

Sasagawa, Y., Nikaido, I., Hayashi, T., Danno, H., Uno, K.D., Imai, T., and Ueda, H.R. (2013). Quartz-Seq: a highly reproducible and sensitive single-cell RNA sequencing method, reveals non-genetic gene-expression heterogeneity. Genome

Biol 14, R31. 10.1186/gb-2013-14-4-r31.

Sato, K., Lee, J.W., Sakamoto, K., Iimura, T., Kayamori, K., Yasuda, H., Shindoh, M., Ito, M., Omura, K., and Yamaguchi, A. (2013). RANKL synthesized by both stromal cells and cancer cells plays a crucial role in osteoclastic bone resorption induced by oral cancer. Am J Pathol 182, 1890-1899. 10.1016/j.ajpath.2013.01.038.

Satomura, K., Tobiume, S., Tokuyama, R., Yamasaki, Y., Kudoh, K., Maeda, E., and Nagayama, M. (2007). Melatonin at pharmacological doses enhances human osteoblastic differentiation in vitro and promotes mouse cortical bone formation in vivo. J Pineal Res 42, 231-239. 10.1111/j.1600-079X.2006.00410.x.

Schindeler, A., McDonald, M.M., Bokko, P., and Little, D.G. (2008). Bone remodeling during fracture repair: The cellular picture. Semin Cell Dev Biol 19, 459-466. 10.1016/j.semcdb.2008.07.004.

Shah, A.N., Davey, C.F., Whitebirch, A.C., Miller, A.C., and Moens, C.B. (2015). Rapid reverse genetic screening using CRISPR in zebrafish. Nat Methods 12, 535-540. 10.1038/nmeth.3360.

Shalhoub, V., Elliott, G., Chiu, L., Manoukian, R., Kelley, M., Hawkins, N., Davy, E., Shimamoto, G., Beck, J., Kaufman, S.A., et al. (2000). Characterization of osteoclast precursors in human blood. Br J Haematol 111, 501-512. 10.1046/j.1365-2141.2000.02379.x.

Shang, E.H., and Zhdanova, I.V. (2007). The circadian system is a target and modulator of prenatal cocaine effects. PLoS One 2, e587. 10.1371/journal.pone.0000587.

Sharif, F., de Bakker, M.A., and Richardson, M.K. (2014). Osteoclast-like Cells in Early Zebrafish Embryos. Cell J 16, 211-224.

Sims, N.A., and Martin, T.J. (2014). Coupling the activities of bone formation and

resorption: a multitude of signals within the basic multicellular unit. Bonekey Rep 3, 481. 10.1038/bonekey.2013.215.

Sire, J.-Y., Huysseune, A., and Meunier, F.J. (1990). Osteoclasts in teleost fish: Light-and electron-microscopical observations. Cell Tissue Res 260, 10. https://doi.org/10.1007/BF00297493.

Sire, J.Y., and Akimenko, M.A. (2004). Scale development in fish: a review, with description of sonic hedgehog (shh) expression in the zebrafish (Danio rerio). Int J Dev Biol 48, 233-247. 10.1387/ijdb.15272389.

Sire, J.Y., Allizard, F., Babiar, O., Bourguignon, J., and Quilhac, A. (1997). Scale development in zebrafish (Danio rerio). J Anat 190 (Pt 4), 545-561. 10.1046/j.1469-7580.1997.19040545.x.

Sousa, S., Afonso, N., Bensimon-Brito, A., Fonseca, M., Simões, M., Leon, J., Roehl, H., Cancela, M.L., and Jacinto, A. (2011). Differentiated skeletal cells contribute to blastema formation during zebrafish fin regeneration. Development 138, 3897-3905. 10.1242/dev.064717.

Soysa, N.S., and Alles, N. (2019). Positive and negative regulators of osteoclast apoptosis. Bone Rep 11, 100225. 10.1016/j.bonr.2019.100225.

Stepensky, P., Grisariu, S., Avni, B., Zaidman, I., Shadur, B., Elpeleg, O., Sirin, M., Hoenig, M., Schuetz, C., Furlan, I., et al. (2019). Stem cell transplantation for osteopetrosis in patients beyond the age of 5 years. Blood Adv 3, 862-868. 10.1182/bloodadvances.2018025890.

Stewart, S., Gomez, A.W., Armstrong, B.E., Henner, A., and Stankunas, K. (2014). Sequential and opposing activities of Wnt and BMP coordinate zebrafish bone regeneration. Cell Rep 6, 482-498. 10.1016/j.celrep.2014.01.010.

Suda, T., Takahashi, N., Udagawa, N., Jimi, E., Gillespie, M.T., and Martin, T.J. (1999). Modulation of osteoclast differentiation and function by the new members of the tumor necrosis factor receptor and ligand families. Endocr Rev 20, 345-357. 10.1210/edrv.20.3.0367.

Suzuki, N., Danks, J.A., Maruyama, Y., Ikegame, M., Sasayama, Y., Hattori, A., Nakamura, M., Tabata, M.J., Yamamoto, T., Furuya, R., et al. (2011). Parathyroid hormone 1 (1-34) acts on the scales and involves calcium metabolism in goldfish. Bone 48, 1186-1193. 10.1016/j.bone.2011.02.004.

Suzuki, N., and Hattori, A. (2002). Melatonin suppresses osteoclastic and osteoblastic activities in the scales of goldfish. J Pineal Res 33, 253-258.

Suzuki, N., Suzuki, T., and Kurokawa, T. (2000). Suppression of osteoclastic activities by calcitonin in the scales of goldfish (freshwater teleost) and nibbler fish (seawater teleost). Peptides 21, 115-124.

Sözen, T., Özışık, L., and Başaran, N. (2017). An overview and management of osteoporosis. Eur J Rheumatol 4, 46-56. 10.5152/eurjrheum.2016.048.

Takeyama, K., Chatani, M., Inohaya, K., and Kudo, A. (2016). TGFβ-2 signaling is essential for osteoblast migration and differentiation during fracture healing in medaka fish. Bone 86, 68-78. 10.1016/j.bone.2016.03.001.

Takeyama, K., Chatani, M., Takano, Y., and Kudo, A. (2014). In-vivo imaging of the fracture healing in medaka revealed two types of osteoclasts before and after the callus formation by osteoblasts. Dev Biol 394, 292-304. 10.1016/j.ydbio.2014.08.007.

Tao, S.C., and Guo, S.C. (2019). Extracellular vesicles in bone: "dogrobbers" in the "eternal battle field". Cell Communication and Signaling 17, 6. 10.1186/s12964-

019-0319-5.

Teitelbaum, S.L. (2000). Bone resorption by osteoclasts. Science 289, 1504-1508. 10.1126/science.289.5484.1504.

Tiedemann, K., Le Nihouannen, D., Fong, J.E., Hussein, O., Barralet, J.E., and Komarova, S.V. (2017). Regulation of Osteoclast Growth and Fusion by mTOR/raptor and mTOR/rictor/Akt. Front Cell Dev Biol 5, 54. 10.3389/fcell.2017.00054.

Tkach, M., and Théry, C. (2016). Communication by Extracellular Vesicles: Where We Are and Where We Need to Go. Cell 164, 1226-1232. 10.1016/j.cell.2016.01.043.

Traver, D., Paw, B.H., Poss, K.D., Penberthy, W.T., Lin, S., and Zon, L.I. (2003). Transplantation and in vivo imaging of multilineage engraftment in zebrafish bloodless mutants. Nat Immunol 4, 1238-1246. 10.1038/ni1007.

Tsuchie, H., Miyakoshi, N., Kasukawa, Y., Aonuma, H., and Shimada, Y. (2013). Intermittent administration of human parathyroid hormone before osteosynthesis stimulates cancellous bone union in ovariectomized rats. Tohoku J Exp Med 229, 19-28. 10.1620/tjem.229.19.

Tu, K.N., Lie, J.D., Wan, C.K.V., Cameron, M., Austel, A.G., Nguyen, J.K., Van, K., and Hyun, D. (2018). Osteoporosis: A Review of Treatment Options. P T 43, 92-104.

Turchinovich, A., Drapkina, O., and Tonevitsky, A. (2019). Transcriptome of Extracellular Vesicles: State-of-the-Art. Front Immunol 10, 202. 10.3389/fimmu.2019.00202.

Udagawa, N., Takahashi, N., Akatsu, T., Tanaka, H., Sasaki, T., Nishihara, T., Koga, T., Martin, T.J., and Suda, T. (1990). Origin of osteoclasts: mature monocytes and macrophages are capable of differentiating into osteoclasts under a suitable microenvironment prepared by bone marrow-derived stromal cells. Proc Natl Acad

Sci U S A 87, 7260-7264. 10.1073/pnas.87.18.7260.

Vahle, J.L., Sato, M., Long, G.G., Young, J.K., Francis, P.C., Engelhardt, J.A., Westmore, M.S., Linda, Y., and Nold, J.B. (2002). Skeletal changes in rats given daily subcutaneous injections of recombinant human parathyroid hormone (1-34) for 2 years and relevance to human safety. Toxicol Pathol 30, 312-321. 10.1080/01926230252929882.

Valenti, M.T., Marchetto, G., Mottes, M., and Dalle Carbonare, L. (2020). Zebrafish: A Suitable Tool for the Study of Cell Signaling in Bone. Cells 9. 10.3390/cells9081911.

van Niel, G., D'Angelo, G., and Raposo, G. (2018). Shedding light on the cell biology of extracellular vesicles. Nat Rev Mol Cell Biol 19, 213-228. 10.1038/nrm.2017.125.

Varshney, G.K., Pei, W., LaFave, M.C., Idol, J., Xu, L., Gallardo, V., Carrington, B., Bishop, K., Jones, M., Li, M., et al. (2015). High-throughput gene targeting and phenotyping in zebrafish using CRISPR/Cas9. Genome Res 25, 1030-1042. 10.1101/gr.186379.114.

Wang, X., Liang, T., Zhu, Y., Qiu, J., Qiu, X., Lian, C., Gao, B., Peng, Y., Liang, A., Zhou, H., et al. (2019). Melatonin prevents bone destruction in mice with retinoic acid-induced osteoporosis. Mol Med 25, 43. 10.1186/s10020-019-0107-0.

Weigele, J., and Franz-Odendaal, T.A. (2016). Functional bone histology of zebrafish reveals two types of endochondral ossification, different types of osteoblast clusters and a new bone type. J Anat 229, 92-103. 10.1111/joa.12480.

Witten, P.E., Harris, M.P., Huysseune, A., and Winkler, C. (2017). Small teleost fish provide new insights into human skeletal diseases. Methods Cell Biol 138, 321-346. 10.1016/bs.mcb.2016.09.001.

Wlodkowic, D., Skommer, J., and Darzynkiewicz, Z. (2009). Flow cytometry-based apoptosis detection. Methods Mol Biol 559, 19-32. 10.1007/978-1-60327-017-5_2.

Wu, R.S., Lam, I.I., Clay, H., Duong, D.N., Deo, R.C., and Coughlin, S.R. (2018). A Rapid Method for Directed Gene Knockout for Screening in G0 Zebrafish. Dev Cell 46, 112-125.e114. 10.1016/j.devcel.2018.06.003.

Yoshikubo, H., Suzuki, N., Takemura, K., Hoso, M., Yashima, S., Iwamuro, S., Takagi, Y., Tabata, M.J., and Hattori, A. (2005). Osteoblastic activity and estrogenic response in the regenerating scale of goldfish, a good model of osteogenesis. Life Sci 76, 2699-2709. 10.1016/j.lfs.2004.10.063.

Zhang, L., Su, P., Xu, C., Chen, C., Liang, A., Du, K., Peng, Y., and Huang, D. (2010). Melatonin inhibits adipogenesis and enhances osteogenesis of human mesenchymal stem cells by suppressing PPARγ expression and enhancing Runx2 expression. J Pineal Res 49, 364-372. 10.1111/j.1600-079X.2010.00803.x.

Zhang, T., Han, W., Zhao, K., Yang, W., Lu, X., Jia, Y., Qin, A., and Qian, Y. (2019). Psoralen accelerates bone fracture healing by activating both osteoclasts and osteoblasts. FASEB J 33, 5399-5410. 10.1096/fj.201801797R.

Zhang, Z., Zhang, Y., Zhou, Z., Shi, H., Qiu, X., Xiong, J., and Chen, Y. (2017). BDNF regulates the expression and secretion of VEGF from osteoblasts via the TrkB/ERK1/2 signaling pathway during fracture healing. Mol Med Rep 15, 1362-1367. 10.3892/mmr.2017.6110.

Zhou, L., Chen, X., Yan, J., Li, M., Liu, T., Zhu, C., Pan, G., Guo, Q., Yang, H., Pei, M., and He, F. (2017). Melatonin at pharmacological concentrations suppresses osteoclastogenesis via the attenuation of intracellular ROS. Osteoporos Int 28, 3325-3337. 10.1007/s00198-017-4127-8.

Zhou, Y., Wang, C., Si, J., Wang, B., Zhang, D., Ding, D., Zhang, J., and Wang, H. (2020). Melatonin up-regulates bone marrow mesenchymal stem cells osteogenic action but suppresses their mediated osteoclastogenesis via MT. Br J Pharmacol. 10.1111/bph.14972.

Zhu, S., Yao, F., Qiu, H., Zhang, G., Xu, H., and Xu, J. (2018). Coupling factors and exosomal packaging microRNAs involved in the regulation of bone remodelling. Biol Rev Camb Philos Soc 93, 469-480. 10.1111/brv.12353.

Acknowledgements

This work would not have been accomplished without the help and support of a lot of individuals. First, I wish to express my deepest gratitude to my supervisors, Professor Yamaguchi and Associate Professor Kobayashi, for offering me an opportunity for this work. I really appreciate their guidance and great advice that always save me from frustration caused by failure or mistakes in the experiment.

I am deeply grateful to Professor Suzuki, Professor Hattorti, Professor Kitamura, and Associate Professor Ikegame for their kindly help and comments with my work. I was astonished to find the beauty of fish scales in the first meeting on Fish Scale Research, which was the beginning of this work. I warmly thank Ph. D. Kanako Lewis for critical evaluation of my manuscripts. I also thank the former and present lab members, Kondo-san, Yamamori-san, Hirakawa-san, Fujita-san, Wada-san, Kimura-san, Otoshi-san, and Hatta-san for their support to the work. I would like to thank my committee members, Professor Suzuki, Professor Takeuchi, Professor Matsubara, and Professor Sekiguchi for their comprehensive questions and encouraging comments on my thesis debate.
Last, special love and gratitude were presented to my loved family for their understanding and support throughout the time.